



Highly active catalysis of methanol oxidative carbonylation over nano Cu₂O supported on micropore-rich mesoporous carbon

Jiajun Wang^a, Tingjun Fu^a, Fanhui Meng^a, Dan Zhao^a, Steven S.C. Chuang^b, Zhong Li^{a,*}

^a State Key Laboratory of Clean and Efficient Coal Utilization, Taiyuan University of Technology, 79 Yingze West Street, Taiyuan 030024, Shanxi, China

^b Department of Polymer Science, The University of Akron, 170 University Avenue, OH 44325, United States

ARTICLE INFO

Keywords:

Nano Cu₂O catalyst
Micropore-rich mesoporous carbon
Methanol
Oxidative carbonylation
Dimethyl carbonate

ABSTRACT

A micropore-rich mesoporous carbon (MMC) derived from ordered mesoporous carbon (OMC) is fabricated as support to prepare a highly active nano Cu₂O catalyst for methanol oxidation carbonylation. The well-dispersed ~3.3 nm Cu nanoparticles with ca. 90% purity of Cu₂O are obtained. The space-time yield and turnover frequency of DMC are significantly enhanced to 34.2 g g_{Cu}⁻¹ h⁻¹ and 89.1 h⁻¹, both of which are greater than that over the mesoporous-only Cu/OMC catalyst. It is found that plentiful under-coordinated carbon atoms are formed in the introduced micropores, which serve as binding sites to immobilize Cu precursors to form the well-dispersed Cu nanoparticles. A large number of these atoms are favorable to accelerate auto-reduction of CuO to Cu₂O in kinetics and further promote to form high-purity Cu₂O. Besides, the electrons of Cu₂O are forced to transfer to the micropore surrounding, forming an electron-deficient Cu⁺ site in favor of intrinsic activity enhancement.

1. Introduction

Dimethyl carbonate (DMC) is such an environment-friendly chemical, which is widely used as nontoxic intermediate for methylation [1], carbonylation [2] and transesterification reaction [3,4], and a fuel additive to improve combustion and reduce engine emissions [5], as well as green solvent in coating, adhesives and electrolytes [6]. Lots of routes have been developed to synthesize DMC with different feedstocks, such as phosgene, methyl nitrite, ethylene (propylene) carbonate, or urea [7]. Among these, the oxidative carbonylation of methanol with O₂ and CO to DMC is highly atom-economical and clean due to the water as the only by-product, so called “green route” [7], and the reaction is more thermodynamically favorable rather than others [8]. It is found that CuCl is the most efficient catalyst, but in the reacting process, the chlorine is easy to form HCl causing chlorine loss [9], which makes the industrial application suffer from several environmental drawbacks, such as chlorine-containing wastewater, equipment corrosion, and product purification as well as catalyst deactivation [10]. To develop chlorine-free Cu-based catalysts has drawn considerable attentions in recent years.

Nano Cu catalyst supported on porous carbon has shown potential as one of candidates for the chlorine-free Cu-based catalyst, which is often prepared by impregnation with nitrate or acetate of copper as chlorine-

free copper source [7,8]. The activated carbon (AC) supporting Cu catalyst was reported to reach 229 mg g_{Cat}⁻¹ h⁻¹ of DMC space-time yield based on per unit of catalyst (STY_{cat}) [11]. If converted to the STY based on per unit of Cu (STY_{Cu}), it is calculated as 2.4 g g_{Cu}⁻¹ h⁻¹ for Cu/AC catalyst. However, it was characterized that the Cu particles in the catalyst seriously agglomerate with average particle size as large as 12.0 nm [11], which far exceeds the AC micropore diameter (<1nm). It thus indicated that the as-formed Cu particles only located at the scarce external surface of AC rather than the inner surface of micropores. But, the ordered mesoporous carbon (OMC), rich in uniform mesopores with large mesopore surface, was reported to confine Cu nanoparticles as small as average 2.9 nm in the mesoporous channels. Even so, the STY_{Cu} over this Cu/OMC catalyst was calculated as only 1.8 g g_{Cu}⁻¹ h⁻¹ [12]. The similar result was observed with mesoporous carbon spheres (MCS) as support. It was found that ~2.0 nm Cu nanoparticles were uniformly dispersed inside the mesopores, but STY_{Cu} was only 2.3 g g_{Cu}⁻¹ h⁻¹ [13]. A fact is clearly shown that the DMC yield in the methanol oxidative carbonylation failed to be enhanced even if the Cu particles are highly dispersed as small as 2.0 nm.

Except for the Cu particle dispersion, the oxidation state of Cu particles also influences the catalytic activity in the methanol oxidative carbonylation. It was shown that the Cu₂O is the most efficient active

* Corresponding author.

E-mail address: lizhong@tyut.edu.cn (Z. Li).

<https://doi.org/10.1016/j.apcatb.2021.120890>

Received 2 August 2021; Received in revised form 28 October 2021; Accepted 31 October 2021

Available online 6 November 2021

0926-3373/© 2021 Elsevier B.V. All rights reserved.

species for the reaction [14]. On the carbon supports, Cu₂O is formed from CuO auto-reduction by the carbon itself, and even over-reduced to metallic Cu under thermal treatment. In the reported Cu/AC catalyst, most of CuO was auto-reduced to not only Cu₂O but also partial metallic Cu with 11.0% Cu loading calcinated at 350 °C [14]. But only 45.5% of CuO was auto-reduced to Cu₂O in the above Cu/OMC catalyst at a low Cu loading of 8.7% [12] and 60.2% in Cu/MCS catalyst at 9.4% Cu loading [13] under the same treating condition. Besides, only 44.5% of CuO was auto-reduced to Cu₂O for Cu particles of 3.0 nm confined in the inner mesopores of carbon nanotube (CNT) at 7.1% Cu loading [15]. It is obvious that the auto-reduction from CuO to Cu₂O is more difficult on those mesoporous carbon supports than that on microporous AC, which inspires that the micropores in AC material play a role in the auto-reduction behavior to form active Cu₂O species, further influence the DMC yield.

Moreover, if the turnover frequency (TOF) of DMC based on a single surface Cu⁺ site calculated, the Cu/AC catalyst shows TOF value as 32.4 h⁻¹, which is significantly higher than 8.3 h⁻¹ for the Cu/OMC catalyst [12] and 6.7 h⁻¹ for the Cu/MCS catalyst [13]. It is clearly shown that one Cu⁺ site supported on microporous carbon materials give much higher catalytic activity than that supported on mesoporous carbon materials. It reveals that the micropores are also particularly relevant to the chemical environment of the as-formed Cu⁺ sites to influence the catalytic activity.

Therefore, it is valuable to prepare a micropores-rich mesoporous carbon (MMC) supporting nano Cu catalyst to improve the catalytic performance in the methanol oxidative carbonylation. And the effect of the micropores on the formation of the Cu₂O species and its special role in the chemical environment of the as-formed Cu⁺ sites are so desired to be investigated.

2. Materials and methods

2.1. Chemicals

The commercial AC (1643 m² g⁻¹) made from coconut shells is purchased from Xinsen Chemical Industry Co., Ltd. The hard template SBA-15 (XFF01, 550–600 m² g⁻¹, 0.65–0.7 cm³ g⁻¹, relative crystallinity ≥ 90%) was purchased in bulk from Nanjing XFNANO Materials Tech. Co., Ltd. The water used was double-distilled. The H₂SO₄ (98 wt %), HF (35.35 wt%), HNO₃ (65–68 wt%) solution, KOH, Cu (NO₃)₂·3H₂O and methanol were manufactured by Tianjin Kermel Chemical Reagent Co., Ltd. Among, HF solution is so dangerous for its hypertoxicity and corrosivity that the protection for respiratory system, eyes and skin is required and the handling is suggested at a hermetic or drafty cabinet. The sucrose and quartz sands were buy from Tianjin Guangfu Fine Chemical Research Institute. All chemicals were of analytical grade and used without any further purification. The pure CO and O₂ (both > 99.999%) gases in the experiments were purchased from Taiyuan Fujiang Special Gas Co., Ltd., and the mixed gases were purchased from Beijing ZG Special Gases Science & Technology Co., Ltd.

2.2. Preparation of MMC supports and Cu/MMC catalysts

The pristine OMC was prepared via the hard-template method [16], except for modifying the terminal graphitized time to 6 h at 900 °C in N₂ atmosphere. The MMC supports were prepared by introducing micropores to the pristine OMC via popular KOH etching, whose mechanism is generally considered as following reaction, 2 KOH + C → 2 K + CO₂ + H₂↑ [17,18]. Firstly, the pristine OMC (1.0 g) was treated with HNO₃ solution (0.5 M) at 80 °C for 4 h to improve the hydrophilicity of the OMC surface for improving KOH dispersion. Then the sample was washed with ample amount of water until pH = 7 is reached for filtrate and then dried at 80 °C overnight. Secondly, KOH was impregnated on the acid-treated OMC by using 40 mL KOH solution at a mass ratio of KOH/OMC = 1–6 under continuous stirring for 6 h. After drying

overnight at 80 °C, the sample was finely ground and calcinated at 800 °C for 1 h at 5 °C min⁻¹ under N₂ to generate micropores. Thirdly, to remove the generated potassium compounds, such as K₂CO₃ and K₂O, and accompanying basic groups on the surface, the sample was first washed with water to pH = 7 and then rinsed with 100 mL of 1 M HNO₃ solution for 4 h, followed by washing with water to pH = 7. After drying at 60 °C overnight, the OMC with different microporosity were obtained as micropore-rich mesoporous carbon (MMC-X) with yields of 47–64 wt %, where X is denoted as the mass ratio of KOH/OMC. A control OMC sample was prepared by treating the pristine OMC similarly as described above except that no KOH was added in the impregnation and denoted as OMC. Another control AC was prepared by washing the commercial AC with 100 mL of 1 M HNO₃ solution for 4 h and then with water to pH = 7 before drying.

As-prepared carbon materials were impregnated into an aqueous solution of Cu(NO₃)₂, stirring at room temperature for 7 h and subsequently drying at hypothermal 50 °C overnight. Then, the precursors were calcined under 350 °C at 2 °C min⁻¹ for 4 h in N₂ atmosphere to obtain the Cu/MMC catalysts with 12 wt.% of Cu loading.

2.3. Characterization techniques

N₂ physisorption was conducted at Micromeritics ASAP2020C apparatus at -196 °C. In advance, the samples were evacuated to vacuum at 350 °C for 8 h firstly to remove the water and impurities at the material surface. The total pore volume and total surface area were calculated by transferring from the N₂ adsorption volume at P/P₀ = 0.95 and the Brumauer–Emmett–Teller (BET) method, respectively. The micropore volume and the surface area of micropore were calculated by t-plot method with a relative pressure P/P₀ of 0.3–0.5 [19]. The volume of mesopore was calculated by subtracting t-plot micropore volume from total pore volume. And the surface area of total external and mesopore channel was calculated by subtracting t-plot micropore area from BET surface area. The pore size distributions at micropore and mesopore regions were determined by Horvath-Kawazoe (H-K) method and Barrett-Joyner-Halenda (BJH) method, respectively.

X-Ray Powder Diffraction (XRD) was conducted on Rigaku D/max2500 X-ray diffractometer with Cu Kα radiation (λ = 0.154056 nm). Small-angle patterns for supports range from 0.5° to 5° with a scanning rate of 0.5 min⁻¹ and a step length of 0.002°. Wide-angle patterns for catalyst range from 10° to 85° with a scanning rate of 4 min⁻¹ and a step length of 0.01°.

X-ray Photoelectron Spectroscopy (XPS) was performed at Thermo Scientific ESCAL AB 250 Xi instrument. The powder samples were adhered on conductive bilateral adhesive and exposed in vacuum below 10⁻⁷ Pa overnight. Then, the sample was transferred to the vacuum analysis chamber for measurement with the X-ray aroused from the monochromatic Al Kα anode. The spectra were calibrated with the C1s spectrum at 284.6 eV and further fitted with 80% Gaussian-Lorentzian ratio at XPSPEAK software.

Elemental Analysis (EA) was carried out at Elementar Analysensysteme (Germany). The samples were decomposed over an WO₃ catalyst under 3%O₂/He flow at 980 °C to form gas mixture (containing CO₂, H₂O, SO₂, NO_x, O₂). Then the resulted gas carried by Helium was inlet to an adsorption system, where the CO₂, H₂O, SO₂ were adsorbed provisionally. And the residual NO_x and O₂ were further inlet to a reduction furnace containing metallic Cu, where NO_x was reduced to N₂ that was detected by TCD and O₂ was absorbed by Cu. Subsequently, the as-adsorbed CO₂, H₂O, SO₂ were desorbed with a temperature programmed ramp and detected by TCD. The absolute content of C, H, N, S was calculated by calibrating the TCD signal with the sample mass. Finally, the O content was obtained by subtracting the total percentages of C, H, N, S from 100%.

Atomic Absorption Spectroscopy (AAS) was conducted on SpectraAA-220 instrument. 200 mg of samples were pre-calcinated under air atmosphere at 600 °C for 6 h to remove the carbon supports. The

remaining samples was completely dissolved in HNO₃ dilute solution and prepared into 250 mL solution. Then 5 mL of this solution was taken and prepared into 100 mL solution further for measuring its absorbance.

H₂-Temperature Programmed Reduction (H₂-TPR) was carried out on Micromeritics AutochemII2920 analyzer as follows: 50 mg of samples were placed in quartz tube and purged with N₂ flow at 300 °C (10 °C min⁻¹) for 30 min firstly. After cooling down to 50 °C, temperature was raised up to 500 °C (10 °C min⁻¹) under 10%H₂/Ar and the real-time signal was recorded with TCD detector. For precise peak assignment, two control samples (CuO/MMC-3 and Cu₂O/MMC-3) were prepared in-situ and further tested for the same H₂-TPR program. The CuO/MMC-3 sample was prepared by oxidizing the as-prepared Cu/MMC-3 with 3%O₂/He mixture at 500 °C for 30 min in-situ. After cooling down to 50 °C, the temperature was programmed up to 500 °C under 10%H₂/Ar for recording TPR pattern. Another Cu₂O/MMC-3 sample was prepared by reducing the as-prepared Cu/MMC-3 with 10% H₂/Ar at 500 °C for 30 min and subsequently oxidizing the sample with N₂O at 60 °C for 30 min to form Cu₂O at the surface of Cu particles. Then, the same TPR program was performed with raising temperature up to 500 °C.

In-situ XRD was carried out on Rigaku SmartLab SE X-ray diffractometer ranging from 5° to 80° with a scanning rate of 8 min⁻¹ and a step length of 0.01°. An in-situ auto-reduction was also conducted on Micromeritics AutochemII2920 analyzer with a branch of exhaust monitored by an online Mass Spectra (MS) using Hiden Hpr20. Firstly, 40 mg of as-impregnated and dried precursors were swept by He flow at 50 °C for 20 min. Since Cu₂(OH)₃NO₃ decomposition on carbon support also generates CO and CO₂ [20], a pre-decomposition step at 200 °C at 10 °C min⁻¹ for 1 h before the auto-reduction was set to avoid signal superposition from decomposition and auto-reduction. After cooled down to 100 °C, it was further raised to 600 °C at 2 °C min⁻¹ and real-time CO and CO₂ emissions were monitored to research the auto-reduction behavior.

Scanning Electron Microscopy (SEM) and transmission electron microscope (TEM) were carried out on JEOL JSM-7800F and JEOL JEM-2100F, respectively. Raman spectra were recorded by a Renishaw inVia micro laser Raman spectrometer (U.K.) stimulated by Ar⁺ laser (wavelength of 514.5 nm) at an output power of 4 mW.

X-ray Absorption Fine Structure (XAFS) of Cu K-edge on Cu/MMC-3 catalyst was characterized with Si (111) crystal monochromators at the BL11B beamlines at Shanghai Synchrotron Radiation Facility. In advance, samples were pressed to thin sheets with diameter of 1 cm and sealed with Kapton tape film. The XAFS spectra were recorded at room temperature by a 4-channel Silicon Drift Detector (SDD, Bruker 5040). The Cu K-edge extended X-ray absorption fine structure (EXAFS) spectra of the as-prepared samples and standard samples (Cu foil, Cu₂O, CuO) were recorded in transmission mode. Negligible changes were observed in the line shape and peak position of Cu K-edge XANES spectra between two scans taken for a specific sample. The data processing was performed on Athena and Artemis programs packed in Demeter 0.9.26, respectively [21].

Room-temperature electron paramagnetic resonance (EPR) was carried out at a fixed microwave frequency of 10.4 GHz on Bruker A300 without light. The spectroscopic splitting factor (g factor) is calculated by the equation: $g = h\nu/\beta B$, in which h is the Planck constant (6.62620×10^{-27} erg/s), β is the Bohr magneton (9.27410×10^{-21} erg/Gs), ν is the microwave frequency (Hz) and B is the resonance magnetic field (Gs).

2.4. Theoretical calculations

All calculations were performed using density functional theory (DFT) method implemented on the Dmol3 code in Accelrys Materials Studio 7.0 package [22]. A $6 \times 6 \times 1$ graphite (0 0 1) supercell is modeled to simulate the surface of the carbon support rich with graphite crystallite. Six types of defects for carbon vacancy, single vacancy (SV),

double vacancy (DV), triple vacancy (TV), quadruple vacancy (QDV) and quintuple vacancy (QTV), are modeled to simulate the as-formed micropores on carbon substrate. Cu₂O nanoparticles were modeled with the (Cu₂O)₂ clusters [23–25]. The vacuum space was set as 20 Å to avoid the interaction between the adjacent graphite layer [26]. The Perdew and Wang (PW91)-type generalized gradient approximation (GGA) functional were utilized to evaluate the nonlocal exchange correlation energy [24]. Double numeric polarized (DNP) basis set was exploited to optimize the graphite layer and Cu₂O nanoclusters. The inner electrons of the graphite and copper atoms were superseded by an effective core potential (ECP). The escape energy (EE_C) of carbon atom on a substrate and the binding energy (BE) of Cu₂O cluster on the support were calculated follows Eqs. 1 and 2, respectively.

$$EE_C = E_{\text{substrate}} - (E_{C1} + E_{(\text{substrate}-C1)}) \quad (1).$$

$$BE_{Cu_2O} = E_{\text{support}} + E_{Cu_2O} - E_{Cu_2O/\text{support}} \quad (2).$$

where $E_{\text{substrate}}$, E_{C1} and $E_{(\text{substrate}-C1)}$ denote the energy for optimized construction of the substrate, one carbon atom, and the substrate with one carbon atom less, respectively. E_{support} and E_{Cu_2O} denote the energy for optimized support and Cu₂O, respectively, while $E_{Cu_2O/\text{support}}$ represents the energy for optimized Cu₂O-support system.

2.5. Catalytic activity tests

The liquid-phase methanol oxidation carbonylation reaction was carried out in a high-pressure continuous stirred slurry bed reactor, of which the operation procedures are expatiated on as follows. Firstly, 0.3 g of catalysts and 30 mL of methanol were added into the kettle sequentially. Then, N₂ flow was inlet to the reactor till 4 MPa lasting for 30 min to check the hermetic seal of the system. After confirming the hermetic seal, N₂ was evacuated and CO and O₂ were successively inlet to the reactor with partial pressure for 2 MPa and 1 MPa, respectively. Stirring speed was set as 300 rpm. Reaction temperature was raised to 110 °C at 2 °C min⁻¹ for 2 h. After cooling down to room temperature, the catalysts and liquid mixture was centrifuged and the supernatant was sucked out for product analysis. And the remained sediment was kept in vacuum at 60 °C overnight to evaporate the residual product in the catalysts channel. After the catalysts were dried, the same processes as above were conducted for another 3 times to test the catalyst stability. Methods of product analysis are given in Supporting Information in detail.

3. Results and discussion

3.1. Textural properties of the MMC supports

The textural properties of the MMC supports resulting from KOH etching are analyzed by N₂ physisorption and the results are summarized in Table 1. As shown, the total pore volume of OMC reaches up to 1.22 cm³ g⁻¹, of which the micropores account for only 0.04 cm³ g⁻¹.

Table 1

Textural properties of the as-prepared MMC supports treated under different mass ratio of KOH/OMC and OMC as well as AC.

Carbon materials	Pore volume (cm ³ g ⁻¹)			Special surface area (m ² g ⁻¹)		
	V _{Tot} ^a	V _{Micro} ^b	V _{Meso} ^c	S _{BET} ^d	S _{Micro} ^e	S _{Ex+Meso} ^f
OMC	1.21	0.04	1.17	1185	62	1123
MMC-1	0.85	0.28	0.57	1384	590	793
MMC-2	0.77	0.32	0.45	1374	756	618
MMC-3	0.61	0.35	0.26	1219	847	372
MMC-4	0.71	0.24	0.47	1312	550	762
MMC-5	1.11	0.27	0.84	1917	585	1332
MMC-6	1.32	0.26	1.06	2174	556	1618
AC	0.72	0.51	0.21	1546	1086	460

^a Total pore volume. ^b Micropore volume. ^c Volume of mesopore. ^d BET surface area. ^e Surface area of micropores. ^f Surface area of external and mesopore.

With KOH/OMC mass ratio increasing from 1 to 3, the total pore volume, mesopore volume and external and mesopore surface area decline, but the micropore volume and area respectively increase from 0.04 to 0.35 $\text{cm}^3 \text{g}^{-1}$ and 62–847 $\text{m}^2 \text{g}^{-1}$. With KOH/OMC mass ratio further increasing from 4 to 6, the micropore volume and area are respectively stabilized at 0.24–0.27 $\text{cm}^3 \text{g}^{-1}$ and 550–585 $\text{m}^2 \text{g}^{-1}$, while the total pore volume, mesopore volume and external and mesopore surface area increase on the contrary. These results suggest that the moderate KOH etching makes the original ordered mesoporous structure degrade and form numerous micropores at low KOH/OMC mass ratio (1–3). While excessive KOH etching does not only generate micropores in the

framework but also results in generating a new mesoporous structure at high KOH/OMC mass ratio (4–6) to varying degrees. As reference, the total pore volume of the commercial AC is 0.72 $\text{cm}^3 \text{g}^{-1}$, of which micropores account for as much as 0.51 $\text{cm}^3 \text{g}^{-1}$.

Based on the above textural properties and morphology of the MMC supports, the evolution of MMC structure resulting from KOH etching is illustrated in Fig. 1. The OMC support presents a closed-packed micron-sized bar-like structure, as shown in Fig. 1a. The carbon bar is composed of plentiful ordered carbon rods (Fig. 1d) which interconnect with each other by a good deal of micro-carbon-bridges [27], as exhibited in the schematic of OMC (Fig. 1g). The ordered mesopores, centered at 3.4 nm

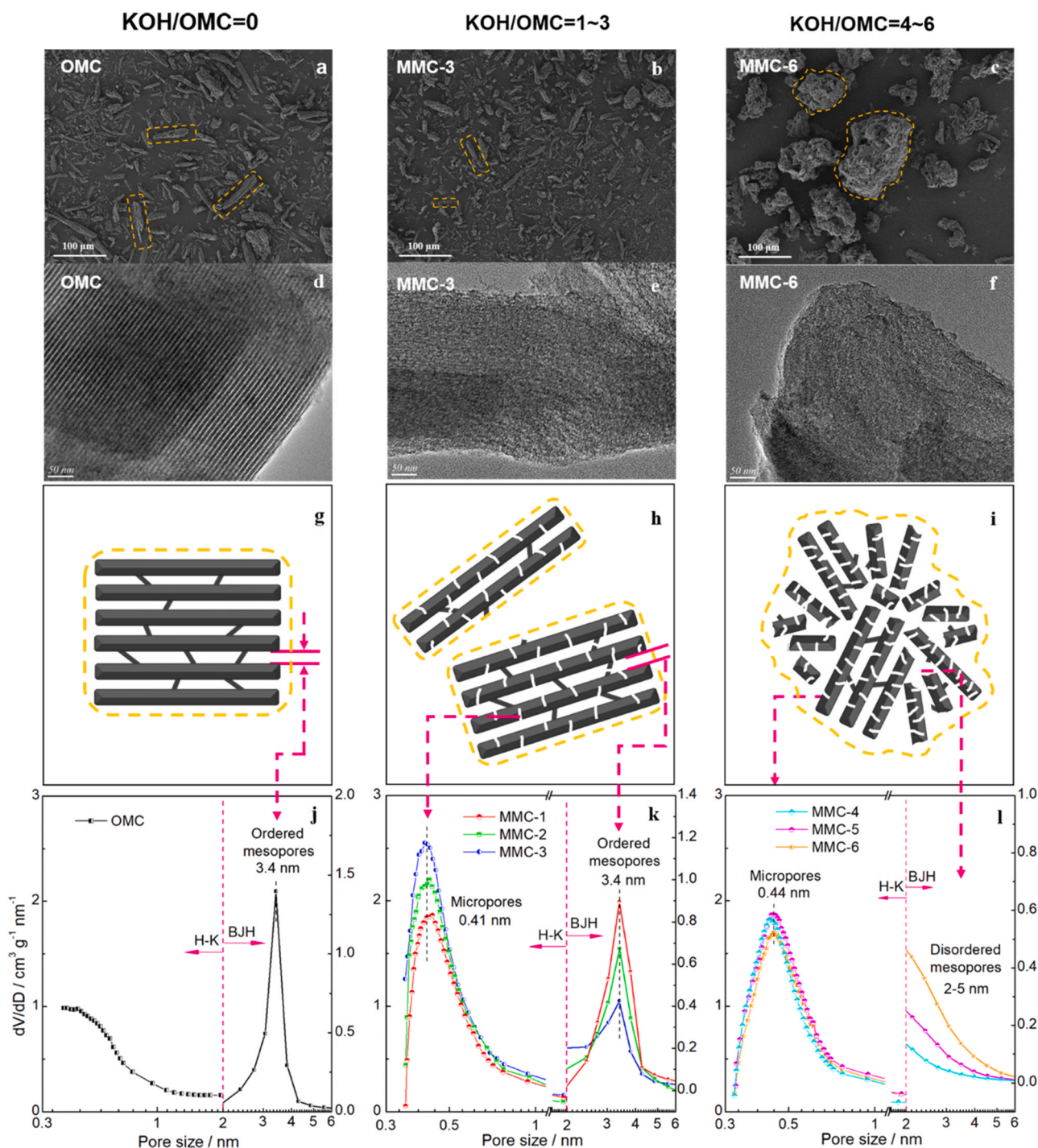


Fig. 1. Illustration for the evolution of MMC structures treated with different KOH/OMC mass ratio. (SEM images (a–c), TEM images (d–f), schematics (g–i) and pore size distribution (j–l)).

as shown in Fig. 1j, are mainly attributed to the space among the carbon rods. As the KOH etching at KOH/OMC = 1–3, the carbon bar structure persists generally with only partially splitting into small particles (Fig. 1b) and the ordered mesoporous structure degrades moderately (Fig. 1e). It is deduced that partial micro carbon-bridges between the carbon rods are likely to be destroyed during etching, as shown in Fig. 1h. Meantime, the pore size distribution (Fig. 1k) suggests that micropores of around 0.41 nm are gradually introduced with the increase in KOH/OMC mass ratio from 1 to 3. However, further increase in the KOH/OMC ratio to 4–6 makes the material aggragate to form some large blocks (Fig. 1c) and the original ordered mesoporous structure further degrade (Fig. 1f) to varying degrees. Especially for the MMC-6 support, block-shaped particles are observed in Fig. 1c, which can also be verified that the as-prepared MMC-6 present sand-like rather than powder-like for other samples in the experimental process. Pore size distribution (Fig. 1l) shows that except for the as-formed micropores of 0.44 nm, disordered mesopores of 2–5 nm size are also formed, while the original ordered mesopores vanish gradually. It suggests that excessive KOH causes increased number of etching sites, which results in some expansion of micropores (MMC-4) and even breaking the carbon rods to irregular fragments (MMC-6). And the ultrafine fragments with different sizes normally connect each other to form large particles [28], as exhibited in Fig. 1i. The newly formed disordered mesopores seem to be attributed to the interstices between accumulated carbon fragments. Even though the KOH etching at weather low or high KOH/OMC ratio makes ordered structure degrade, some short-range ordered structures are still retained. This was supported by the presence of partial carbon rods structures in TEM images (Fig. 1d–f) and the presence of (100) diffraction peak in small-angle XRD patterns (Fig. S1c). In short, the pore structures of MMC supports treated at KOH/OMC ratio from 1 to 3 are generally considered as micropore-rich in the ordered mesopore channel with gradually increasing micropores. While those treated at KOH/OMC ratio from 4 to 6 are summarized as micropore-rich in disordered mesopore channel with increasingly disordered mesopores. As reference,

SEM image of AC support (Fig. S2c) shows that it presents block-shaped structure and there are some obvious mesopores or macropores on AC monoblock. Pore size distribution (Fig. S1b) indicates numerous micropores with size of 0.44 nm, which are always distributed at the bottom of those mesopores or macropores.

The XPS (Table S1 and Fig. S3) and EA results (Table S1) of as-prepared supports suggest that the HNO₃ rinse has generally assimilate the chemical composition and surface functional groups of MMC despite of treating with different KOH/OMC mass ratio. Thus, the variation of the pore structure is used as the single independent variable for following discussion.

3.2. Surface properties of the Cu/MMC catalysts

The dispersion of Cu nanoparticles on the MMC support was observed by TEM images, shown on Fig. 2. The diameter of the supported nanoparticles is calculated by averaging 100 random particles in the image using Nano Measurer software. As a premise, AAS results show that the actual loadings of Cu element on all supports are 11.0–11.8 wt%, as shown in Table 2. It suggests the amount of Cu is almost unaffected by the micropore introduction, which is due to the fact that it is prepared by wetness impregnation. As shown in Fig. 2, the Cu nanoparticles with the diameter of 4.1 nm are homogeneously attached to the carbon rods of OMC support, which is approximate to the pore diameter (3.9 nm) of the support. It suggests that most of the Cu nanoparticles are confined in the ordered mesopores due to the spatial confinement effect. With the introduction of micropores, the size of the Cu nanoparticles is further slightly decreased to 3.8 nm, 3.3 nm and 3.9 nm for Cu/MMC-2, Cu/MMC-3 and Cu/MMC-4, respectively, and the distribution density of the nanoparticles is increased notably. It suggests that micropores provide many immobilized sites for Cu nanoparticles. In other word, the interaction between the nanoparticles with micropore-rich support is stronger than that with micropore-lacked support. It is widely shared that the metal ion always forms complex

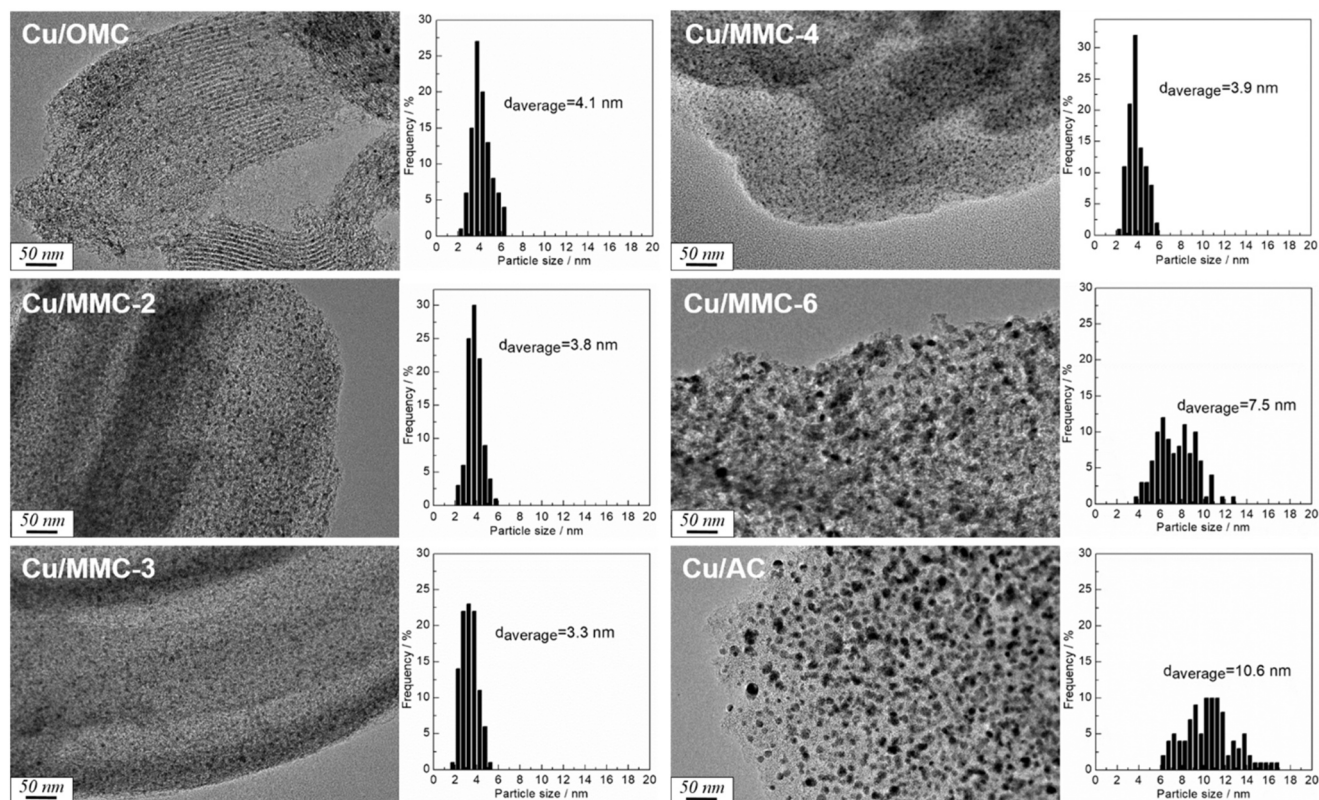


Fig. 2. TEM images of as-prepared catalysts and histograms of Cu particle size distribution.

Table 2

Catalytic performance of Cu/MMC catalysts in methanol oxidative carbonylation.

Catalysts ^a	Cu loading ^b (wt%)	C _{methanol} ^c (%)	S _{DMC} ^d (%)	STY _{cat} ^e (g g _{cat} ⁻¹ h ⁻¹)	STY _{Cu} ^f (g g _{Cu} ⁻¹ h ⁻¹)	TOF ^g (h ⁻¹)	R _D ^h (%)
Cu/OMC ^{1st}	11.5	1.1	96.4	0.6	5.2	29.1	83.3
Cu/OMC ^{4th}	10.6	0.2	94.4	0.1	0.9	–	–
Cu/MMC-2 ^{1st}	11.8	6.4	94.4	3.4	28.8	90.8	24.6
Cu/MMC-2 ^{4th}	10.8	4.6	95.4	2.5	21.2	–	–
Cu/MMC-3 ^{1st}	11.4	7.2	95.1	3.9	34.2	89.1	20.5
Cu/MMC-3 ^{4th}	10.8	5.8	95.6	3.1	27.2	–	–
Cu/MMC-4 ^{1st}	11.0	5.1	94.2	2.7	24.5	85.0	44.5
Cu/MMC-4 ^{4th}	10.2	2.9	93.6	1.5	13.6	–	–
Cu/MMC-6 ^{1st}	11.4	2.0	93.8	1.0	8.8	83.1	79.5
Cu/MMC-6 ^{4th}	10.5	0.3	94.6	0.2	1.8	–	–
Cu/AC ^{1st}	11.0	3.0	96.1	1.6	14.5	114.5	12.4
Cu/AC ^{4th}	9.9	2.6	92.1	1.4	12.7	–	–

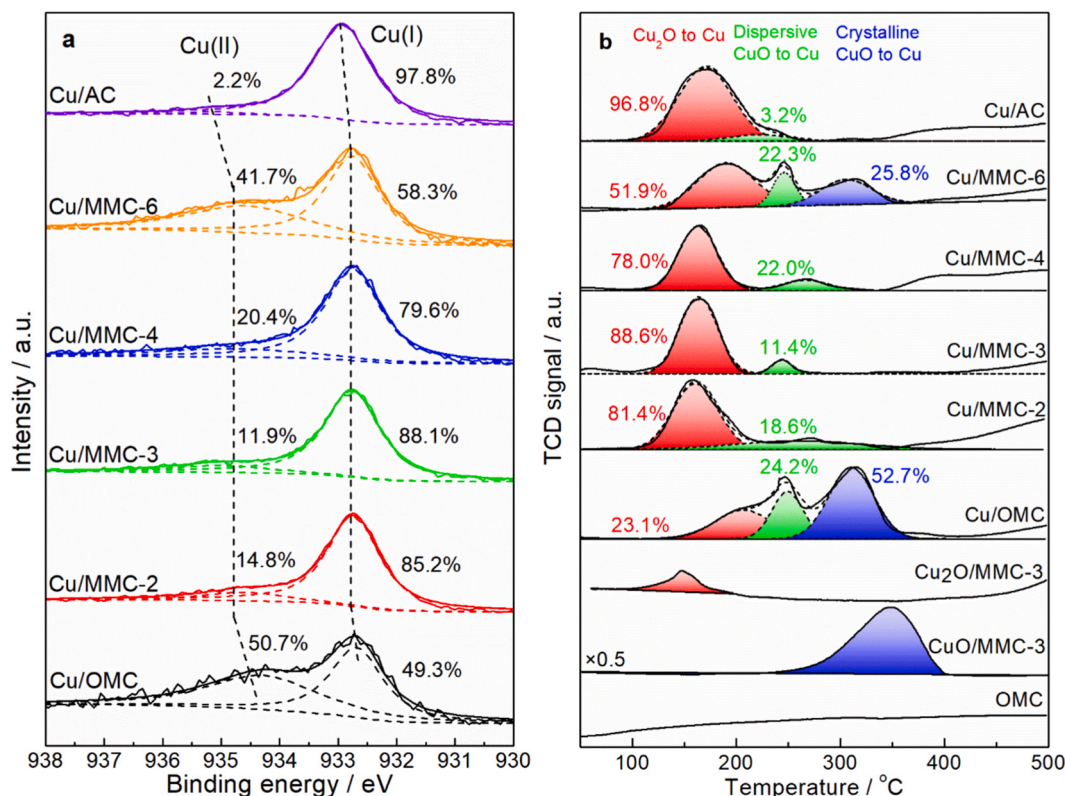
^a Reaction condition: Liquid-phase reaction. Catalyst mass: 0.30 g. P_{CO} = 2.0 MPa, P_{O2} = 1.0 MPa, t = 2 h, T = 110 °C, V_{methanol} = 30 mL, stirring speed = 300 r/min. ^b Actual Cu loading determined by AAS. ^c Conversion of methanol. ^d Selectivity of dimethyl carbonate. ^e Space-time yield of DMC based on per gram of catalyst. ^f Space-time yield of DMC based on per gram of Cu. ^g Turnover frequency of DMC on per surface Cu⁺ site. ^h Deactivation rate of the catalyst.

ion with H₂O molecules in aqueous solution. For example, the Cu²⁺ ions always form Cu(H₂O)₄²⁺ complex ions, the dynamic diameter of which is estimated as 1.5 nm for the Cu(H₂O)₄²⁺ regular tetrahedron [29]. It is inferred that the large impregnated-metal ions diffuse into the mesopores and are captured by the micropores on the mesopore wall during impregnation. And restrained by the internal diffusion resistance of the micropores [30], most of the ions are only located at the micropore mouth. In the further calcination, Cu(H₂O)₄²⁺ ions are decomposed and aggregated together with the adjoining ones to form CuO nanoparticles. The strong interaction between the micropore-rich support and nanoparticles as well as the confinement effect of the mesopores resists the further growth up of the CuO nanoparticles under heating, which gives rise to the small particle size.

However, the excessive destroy of the ordered mesoporous structure and overmuch disordered mesopores give rise to relatively inferior dispersion as the Cu particle size increasing to 7.5 nm for Cu/MMC-6. It

suggests that the overmuch disordered mesopores among the carbon fragments also give some internal diffusion resistance for Cu(H₂O)₄²⁺ ions, which renders most of the Cu(H₂O)₄²⁺ ions located at the external surface of the support to form relatively large particle. Similarly, the large particles of 10.6 nm are immobilized at the micropore mouth on AC support due to the lack of mesopore. In summary, the ordered mesopores in the support are favorable for Cu(H₂O)₄²⁺ ions diffusion and confining the Cu nanoparticles, while the micropores in the mesopore channel take charge of capturing Cu(H₂O)₄²⁺ ions and immobilizing the as-formed Cu nanoparticles. Therefore, the ordered mesoporous structure rich of micropores in the channel yields not only well-dispersed but also stable Cu nanoparticles.

The detailed oxidation state for the Cu species in both surface and bulk are analyzed by Gaussian-fitting the XPS spectra and H₂-TPR patterns, as shown in Fig. 3a and b, respectively. As shown in Fig. 3a, two Gaussian-fitting peaks located at ~932.7 eV and ~934.5 eV are

**Fig. 3.** XPS spectra of Cu_{2p3/2} (a) and H₂-TPR patterns (b) for the catalysts.

assigned to Cu(I)/Cu(0) and Cu(II), respectively. Complementary XAES spectra (Fig. S4a) present only one peak at ~ 570.4 eV attributed to Cu(I) suggesting that there is no metallic Cu in the catalysts, which is consistent with the XRD results (Fig. S4b). It is clearly shown that Cu_2O only accounts for 49.3% in surface as for the Cu/OMC catalyst, but dominates 97.8% in surface for Cu/AC. In Fig. 3b, the parallel results of CuO/MMC-57 and Cu_2O /MMC-57 show that the reduction peak of supported Cu_2O is located at about 170°C , but that of supported CuO nanoparticles is located at $\sim 350^\circ\text{C}$. The absence of crystalline CuO in XRD pattern but a bit of surface CuO in XPS spectrum for Cu/MMC-57 catalyst suggest that the peak at $\sim 250^\circ\text{C}$ is like to be attributed to the reduction of amorphous, or well-dispersed, CuO. This is consistent with the report of Tsubaki [31]. Based on the above ascription, the percentages of Cu_2O , dispersed CuO and crystalline CuO in bulk are calculated and the results are labeled on Fig. 3b. It is found that Cu_2O only accounts for 23.1% in bulk for Cu/OMC but occupies 96.8% in Cu/AC catalyst. Besides, the percentage of both surface and bulk Cu_2O monotonously increases with the increase of micropore volume, as shown in Fig. S4c, which is consistency with the XRD results (Fig. S4b). With the most micropore volume of $0.35\text{ cm}^3\text{ g}^{-1}$, the percentage of Cu_2O in Cu/MMC-3 catalyst reaches up to about 90% whether in surface or bulk of the nanoparticles. The result suggests that the micropores are not conducive to the existence of CuO but favorable for the formation of Cu_2O . As the Cu_2O is generated from auto-reducing CuO by carbon support without additional reductant, the results imply that the introduction of micropores promotes the auto-reduction from CuO to Cu_2O . The percentage of Cu_2O in Cu/MMC-6 catalyst is inconsistent with the law, which is likely due to the most micropores encapsulated in the excessively disordered mesopores. By comparing the Cu/AC with Cu/MMC-6, it is found that even larger particle on AC support yields more Cu_2O than that on MMC-6 support. It further proves that the easy auto-reduction is ascribed to the high microporosity, but not only size effect. It can also be found that the percentage of surface Cu_2O is greater than that of the bulk Cu_2O on micropore-less support, whereas they are similar on micropore-rich support, as shown in Fig. S4c. This result suggests that the surface CuO is easier to be auto-reduced than the bulk CuO, but numerous micropores also facilitate the reduction of bulk CuO. Thus, it is inferred that the reduction of CuO begins with the reduction of surface CuO and subsequently with the deep reduction of bulk CuO.

On the other hand, the binding energy of both Cu species is observed to increase due to the micropores as shown in Fig. 3a, which suggests that the micropores facilitate electron transfer from Cu nanoparticles to carbon support and thus increase their interaction, which is consistent with the inference by TEM images. Stronger binding energy of electron is observed at the Cu/AC catalyst than the as-prepared Cu/MMC catalyst, which may be influenced by various factors, such as size effect originated from electronic functionality or interaction of Cu nanoparticles with some impurities in AC support.

3.3. Catalytic performance of Cu/MMC in methanol oxidative carbonylation

The catalytic performances in methanol oxidation carbonylation over the above Cu/MMC catalysts were evaluated. The methanol conversion (C_{methanol}), selectivity of DMC (S_{DMC}) and space-time yield of DMC based on per unit of catalyst (STY_{cat}) are calculated, as listed in Table 2. As shown, the selectivity of DMC for all catalysts reaches up to over 90% and it is almost stable at 4 successive runs. This result suggests that the DMC selectivity is insensitive to the support properties or Cu dispersion and oxidation state. But it was reported that the low reaction temperature favor DMC formation [32]. The low methanol conversion is an ongoing problem for the methanol oxidative carbonylation. In terms of reaction mechanism, the methanol is firstly oxidized to methoxide group (CH_3O) on the Cu_2O surface. This step is thermodynamically slow, exothermic by only 28.4 kJ mol^{-1} , despite of the promotion in the presence of O_2 [33]. However, it is further facilitated

thermodynamically by the subsequent CO insertion into the as-formed Cu-methoxide to form surface monomethyl carbonate group (CH_3OCO). This insertion is always regarded as the rate-determining step for the overall reaction [34,35]. Once the CH_3OCO group is formed, it is easy to combine with another CH_3O group to form DMC. Thus, the space-time yield of DMC is a comprehensive indicator for evaluating the catalytic activity of the reaction. It is shown that by comparing with Cu/OMC catalyst, the STY_{cat} is increased obviously due to the introduction of micropores. The optimized catalyst, Cu/MMC-3, gives the STY_{cat} up to $3.9\text{ g g}_{\text{cat}}^{-1}\text{ h}^{-1}$ for first cycle, which is ca. 6.5-folds and 2.4-folds as that over the Cu/OMC ($0.6\text{ g g}_{\text{cat}}^{-1}\text{ h}^{-1}$) and Cu/AC ($1.6\text{ g g}_{\text{cat}}^{-1}\text{ h}^{-1}$) catalyst, respectively. This efficient yield of DMC on Cu/MMC catalysts is strongly depended on the high surface area of Cu_2O in the catalyst, as shown in Fig. 4, which confirms that the Cu_2O in the catalysts serves as the active species in the reaction. The inconsistency of Cu/AC and Cu/OMC catalyst will be discussed in aspect of intrinsic activity below.

For comparing with the reported catalysts, the STY based on per unit of Cu (STY_{Cu}) was further calculated, also listed in Table 2. As reported, the STY_{Cu} over the Cu/OMC [12] and the Cu/AC [11] catalysts in gas-phase reaction were $1.8\text{ g g}_{\text{Cu}}^{-1}\text{ h}^{-1}$ and $2.4\text{ g g}_{\text{Cu}}^{-1}\text{ h}^{-1}$, respectively [13]. While those in liquid-phase reaction are calculated as $5.2\text{ g g}_{\text{Cu}}^{-1}\text{ h}^{-1}$ and $14.5\text{ g g}_{\text{Cu}}^{-1}\text{ h}^{-1}$, respectively. The higher value in liquid-phase reaction than the gas-phase reaction is found to be attributed to the methanol solvent thermodynamically as well as kinetically favor CO insertion into methoxide species [36]. More significantly, the STY_{Cu} over the Cu/MMC catalysts are also increased obviously by comparing with the Cu/OMC and Cu/AC catalysts. The optimized catalyst in this work yield DMC as high as $34.2\text{ g g}_{\text{Cu}}^{-1}\text{ h}^{-1}$.

Turnover frequency (TOF) was further calculated for the fresh catalyst to indicate the intrinsic activity for an active Cu^+ site at surface, also listed in Table 2. It is calculated as 29.1 h^{-1} for Cu/OMC, which is much less than 114.5 h^{-1} for Cu/AC. Owing to the micropore introduction, the Cu/MMC-X catalysts exhibit ca. $80\text{--}90\text{ h}^{-1}$ of TOF, which is enhanced obviously by comparing with Cu/OMC catalyst but slightly lower than Cu/AC. Combining with the above analysis of the electron binding energy in XPS spectra, this increase of TOF value is found to be correlated with the increasing electron transfer from Cu nanoparticles to the carbon support. It is likely to suggest that the electron-deficient

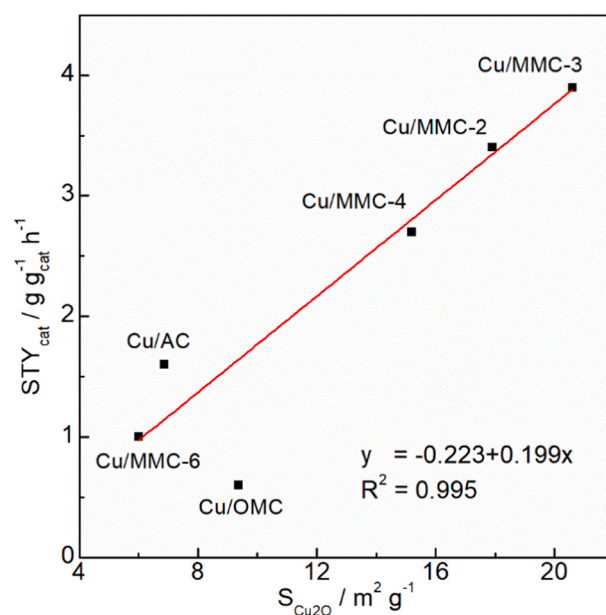


Fig. 4. Relationship between the catalytic activity and the surface area of active Cu_2O species.

environment of the Cu^+ sites is favorable for DMC formation. In terms of mechanism, the reaction is strongly rate-determined by the step of CO insertion into surface methoxide group. This insertion is reported to be facilitated by moderately strengthening the adsorption of CO [37]. As known, CO adsorbs on Cu^+ site is in the form of σ -donor of CO molecule to Cu 4p-derived electronic states [38]. Decreasing electronic density of Cu^+ site is obviously promising to enhance the σ bonding to strengthen CO adsorption and facilitate its insertion. The proposition can also be testified by some other reports [22,26,39]. This conclusion shows a promising strategy to improve the intrinsic activity of methanol oxidation carbonylation by increasing electron transfer from Cu_2O species to supports.

The stability of the catalysts was evaluated through four cycles of test for catalytic activity and the deactivation rates are calculated based on the STY_{cat} of DMC. It is observed that the Cu/OMC catalyst gives inferior stability and the deactivation rate is calculated as 83.3%. With the increase of microporosity, the stability of the catalyst is improved significantly. For the Cu/MMC-3, the deactivation rate is only 20.0%. The Cu/AC catalyst gives the best stability, whose deactivation rate is calculated as only 13.8%. The reason for the deactivation is further explored.

Firstly, the loss of Cu is evaluated by comparing the practical Cu loading in the fresh and used catalysts, as listed in Table 2. The result shows that the Cu loading on the used Cu/MMC-3 catalyst is 10.8%. By comparing with the fresh catalyst (11.4%), the loss rate of Cu is only approx. 5%. Besides, as shown in the TEM images of the used catalysts on Fig. 5a, it is found that the dispersion of the Cu nanoparticles on the used catalyst is almost similar with the fresh catalyst. It can also be reflected by the almost unchanged peak width in XRD patterns. These two aspects of particle stabilization results from not only the micropore immobilization but also the uniform dispersion of the particles and the confinement effect of the mesopore channels.

On the other hand, the variation of the oxidation state is also analyzed. As shown in the Fig. 5b, the XRD patterns of used catalysts show that Cu_2O declines obviously, while CuO and metallic Cu are

present on Cu/OMC catalyst, which indicates the disproportionation of Cu_2O in methanol environment [40]. With the increase of microporosity, the absence of metallic Cu proves that the disproportionation of Cu_2O has been eliminated by increasing the metal-support interaction. Another deactivation reason relies on the Cu_2O oxidation. As shown in the XPS spectra of the used catalysts exhibited in Fig. 5c, CuO is obviously formed on the surface of the used catalysts. By comparing with the results of the fresh catalysts, it clearly suggests that the active Cu_2O species are oxidized to inactive CuO to varying degrees, which is ascribed to the main factor for deactivation. This oxidation of Cu_2O is always spontaneous in the presence of O_2 , because the oxygen atoms appear to dissolve quite easily into the small metal particles [41,42]. Even so, the modification by introducing micropores to the carbon support effectively resists the Cu_2O oxidation, as suggested by the less CuO in Cu/MMC-3 and Cu/AC than Cu/OMC catalyst.

The present results indicate that the abundant surface areas in the ordered mesopores are favorable for dispersing Cu nanoparticles, while micropore is beneficial for forming high-purity Cu_2O and immobilizing it. The good dispersion and high purity make the catalyst expose large number of active sites at the surface, and thus yield a high apparent activity for the catalysis. On the other hand, the micropores also facilitate electron transfer from the as-formed Cu_2O nanoparticles to the carbon supports, which results in a high TOF at each active Cu^+ site and a nice stability in the reaction. Hence, a more efficient catalyst can be realized in terms of further improving the effective surface area of the active Cu_2O or increasing electron transfer to improve the apparent and intrinsic activity, respectively. The work makes an important advance in the development of chlorine-free Cu based catalyst for avoiding the environmental problems due to the CuCl catalyst.

3.4. Mechanistic action of micropores on formation and stabilization of Cu_2O

As above analysis, micropores promote the auto-reduction from CuO

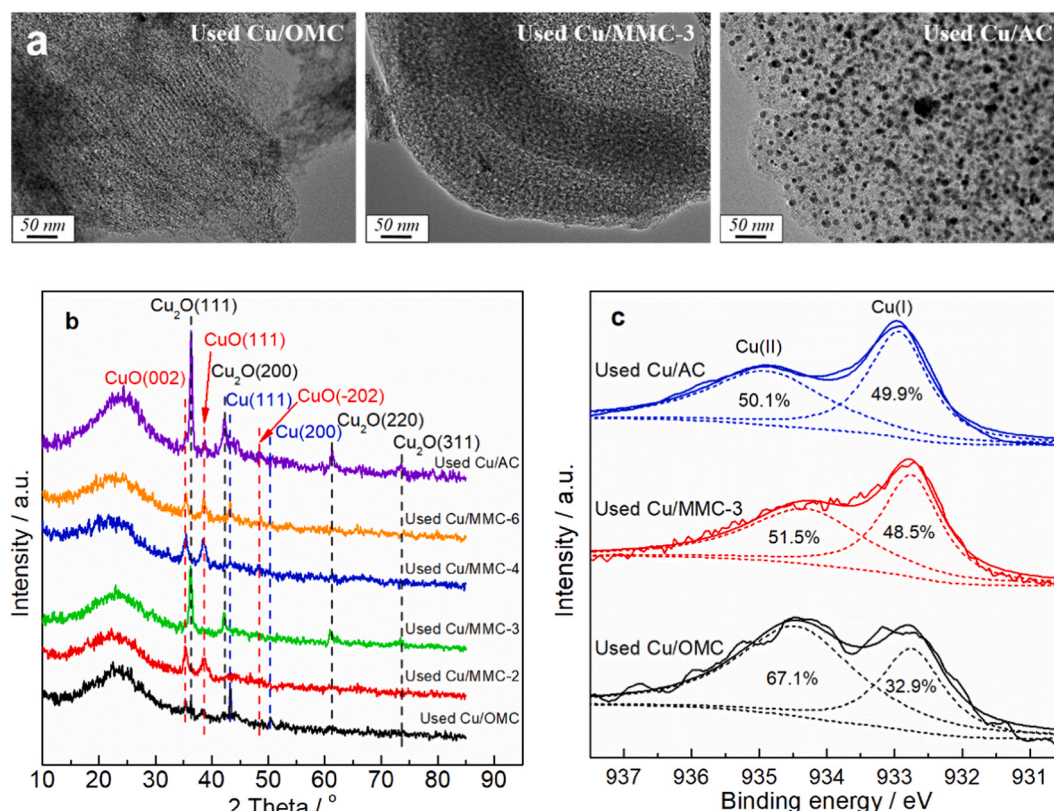
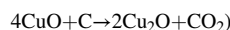


Fig. 5. The analysis for the catalytic deactivation. (a) Representative TEM images, (b) XRD patterns and (c) XPS spectra of the used catalysts.

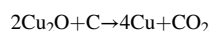
by the carbon support itself, but no similar cases and mechanism has been reported yet. Herein, the auto-reduction behavior was investigated by both in-situ XRD technique and mass spectrometry conducted on Cu/AC, Cu/OMC and Cu/MMC-3 precursors, and the results are shown on Fig. 6. As shown in Fig. 6a-c, the peaks at 12.8° , 25.7° , 33.5° , 36.5° and 43.5° are ascribed to the (001), (002), (120), (121) and (122) lattice planes of $\text{Cu}_2(\text{OH})_3\text{NO}_3$, respectively (JCPDS 54-0747). Taking Cu/AC as an example, these peaks disappear and two main peaks of CuO (35.5° and 38.7° , JCPDS 45-0937) appear at about 200°C simultaneously, which suggests that $\text{Cu}_2(\text{OH})_3\text{NO}_3$ species are rapidly decomposed to CuO at about 200°C . When the temperature reaches up to 225°C , diffraction peaks of CuO start to decline and completely disappear until 300°C . While the peaks of Cu_2O (36.5° , 42.4° and 61.5° , JCPDS 65-3288) gradually dominate. It suggests that CuO is gradually auto-reduced to Cu_2O between 225°C and 300°C . When the temperature further reaches over 300°C , the intensity of diffraction peaks attributed to metallic Cu (43.4° , 50.6° and 74.3° , JCPDS 65-9743) increases gradually. Until 450°C , the Cu_2O peaks vanish completely. The results indicate that Cu_2O is further auto-reduced to metallic Cu by carbon supports between 300°C and 450°C . In a similar way, it is found that CuO is auto-reduced to Cu_2O between 225°C and 350°C for Cu/OMC precursors, while Cu_2O is further auto-reduced to metallic Cu between 300°C and 550°C . The starting temperature of auto-reduction is similar with Cu/AC but the temperature needed for complete reduction is obviously higher than Cu/AC. For Cu/MMC-3 precursor, it is found that CuO is auto-reduced to Cu_2O between $225-300^\circ\text{C}$ and Cu_2O is further auto-reduced to metallic Cu between 300°C and 500°C . The

temperature for complete reduction is obviously decreased as compared with Cu/OMC. The similar starting temperature and different duration of auto-reduction for all samples suggest that the micropore introduction has not changed the mechanism of auto-reduction but obviously increased the reduction rate of CuO to Cu_2O at a certain temperature.

The real-time CO and CO_2 emissions, monitored by online MS during the auto-reduction process of these three precursors as well as MMC-3 support, are shown on Fig. 6d. As shown in the result of MMC-3 support, the emissions of CO and CO_2 before 500°C are almost negligible, while the obvious CO emission beyond 500°C is always ascribed to the decomposition of oxygen-containing functional groups [43]. By contrast, two obvious peaks for CO_2 emission are observed at $200-300^\circ\text{C}$ and $300-500^\circ\text{C}$ for all catalyst precursors. Combined with the results from in-situ XRD, these two peaks are consequently ascribed to the reduction from CuO to Cu_2O and Cu_2O to metallic Cu as Schemes (1) and (2), respectively. Close examination shows that the reduction peaks of both CuO to Cu_2O and Cu_2O to metallic Cu on AC support are so sharp, whereas the same are broad on OMC support despite of the similar central temperature. It suggests that the reduction on OMC substrate is obviously slower than that on AC, which is consistent with the in-situ XRD results. The peak widths of Cu/MMC-3 are significantly narrowing down, which also suggests the micropores favor increasing auto-reducing rate.



Scheme 1



Scheme 2)

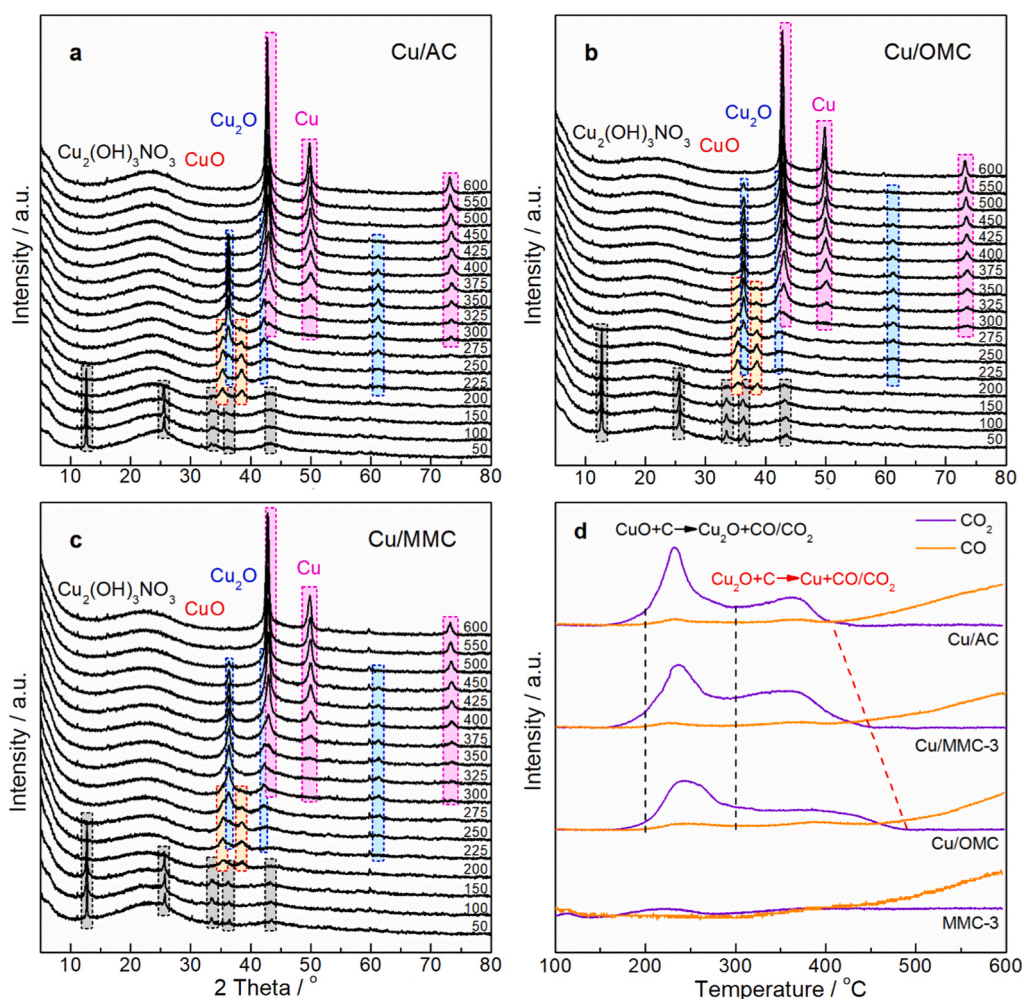


Fig. 6. In-situ XRD patterns (a-c) and CO/ CO_2 emission monitored by online MS (d) of Cu/AC, Cu/OMC and Cu/MMC-3 precursors undergoing auto-reduction.

Known as the Arrhenius formula, rate of a chemical reaction is proportional to the rate constant and reactant concentration, and the rate constant is proportional to reaction temperature but inversely proportional to the activation energy. The mechanism of the reaction is not changed with micropores as above analysis, which suggests the activation energy for auto-reduction with or without micropores is the same. It is thus deduced that at a certain temperature, introducing micropores gives rise to increasing concentration of the reactive carbon atoms to accelerate the reducing rate. Besides, the auto-reduction of CuO by carbon support is such a typical solid-phase reaction, the rate-determined step of which will transform from reaction-controlled to diffusion-controlled after the reaction proceeds for a time [44,45]. This is consistent with the deduction that the auto-reduction starts from surface, followed by deep reduction in bulk. As suggested by well-known Hedvall effect [46], at a certain temperature, a quick crystalline transformation induces a weakening in the lattice and thus provides a greater possibility for the diffusion of lattice atoms, resulting in increasing reactivity of a solid. It suggests that on micropore-rich carbon supports, the rapid auto-reduction of CuO transfer to Cu₂O in the early stage prefers to further facilitate the diffusion of lattice oxygen for deep reduction of bulk CuO. It thus contributes to the high percentage of Cu₂O in both surface and bulk of the nanoparticle on micropore-rich carbon supports.

Two other possible methods can be adopted for attempt to improve the reduction degree of CuO to Cu₂O. One is raising the reducing temperature, but metallic Cu formation and aggregation of Cu₂O nanoparticles is accompanied inevitably, which goes against the original intent to improve effective surface of the Cu₂O species. Another method is extending the duration of constant temperature for reduction. Thus, a particular auto-reduction process was designed appending with a duration for 1 h at 240 °C, as the reaction is speeded up at this temperature as observed in Fig. 6d. The on-line MS result (Fig. S5b) shows that during the constant temperature, the auto-reduction instantly slows down. And with the temperature further rising, the auto-reduction is speeded up again. It reveals that long-time reduction is of no worth for improving the reduction degree, which is due to the diffusion control. By comparing with these two methods, micropores introduction to facilitate Cu₂O formation is proved to be most feasible.

Further to confirm the reactive carbon atoms in the porous carbon supports, an atomic insight is given into the micropore. Raman spectra suggest that introducing micropores results in increase of defects in the material, as shown in Fig. S6. It is noted that during the KOH etching, many types of defects are formed in micropores, such as carbon vacancy defects, armchair edge or zigzag edge defects, covalent interlayer bonds and so on [47]. But vacancy-type defects produced by digging out carbon atoms on the OMC mesoporous wall to form micropores is the main defects, and it is modeled to simulate the as-formed micropores on carbon support, as shown in Fig. 7. And the sizes of these vacancies, as labeled on Fig. 7, are consistent with the pore size distribution of

introduced micropores.

As we know, at the pristine graphite surface, the carbon atoms connect with each other by three σ bonds formed by sp^2 hybridized orbitals, and the residual p electron is perpendicular to the graphite plane, forming a Π bond with the surrounding p electrons. Fig. 7 shows that the single, triple and quintuple vacancy make some adjoining carbon atoms (colored in green) coordinate by only two σ bonds, which will leave a dangling bond at each under-coordinated carbon atom [47]. However, the configuration of double-vacancy and quadruple-vacancy graphite shows that carbon atoms will rearrange to form eight or nine membered rings and new five membered rings (colored in orange). The defective carbon atoms in these two structures are still saturated, combining each other by three σ bonds. The structures of single vacancy and double vacancy are widely shared [47], but little research has reported structures of vacancy with multiple carbon atoms in detail. It is deduced that an odd number of defective carbon atoms will leave under-coordinated carbon atom, while an even number of defective carbon atoms will rearrange to form new rings. Although the number of defective carbon atoms is difficult to be artificially controlled, continuous KOH etching on multi-layers of graphite sheets consequentially results in increase of under-coordinated carbon atoms in the material. Interestingly, a negative potential isosurface (colored by red) is observed at the center of the single, triple and quintuple vacancy, but it is absent at double and quadruple vacancy, as shown in Fig. 8a. This negative potential region seems to be due to the existence of dangling bonds. And it reveals the defective sites are susceptible to electrophilic attack, which can also be deduced that $Cu(H_2O)_4^{2+}$ ions prefer to bind with these under-coordinated carbon atoms during impregnation to form Cu-C bonds.

To demonstrate the reasonability of vacancy-type defects modeling as-formed micropores in carbon support, EPR experiments were conducted on OMC, MMC-3, AC supports and their corresponding catalysts, and the results are shown in Fig. 8b. A single EPR signal resonated at $g = 2.0033$ is observed for all samples, which is attributed to the dangling bonds affiliated to the under-coordinated carbon atoms [48]. The weak EPR signal for OMC support indicates a small number of under-coordinated carbon, which are mainly located at edges of graphite crystallite. Owing to the micropore introduction, the EPR intensity of MMC-3 support has become stronger than OMC, which is similar with that of AC. It suggests that the micropores indeed generate numerous under-coordinated carbon atoms on carbon supports, which sufficiently accounts for the reasonability of the model. Moreover, the EPR intensity of the catalyst is so weaker than the corresponding support, which suggests the Cu₂O loading decreases the quantity of dangling bonds. It clearly testifies that the Cu₂O nanoparticles pair the dangling bonds of the under-coordinated carbon atoms to form Cu-C bond at the interface between Cu₂O nanoparticles and carbon support.

Further to confirm the above deduction, the local structure around the Cu₂O nanoparticles are characterized by synchrotron XAFS

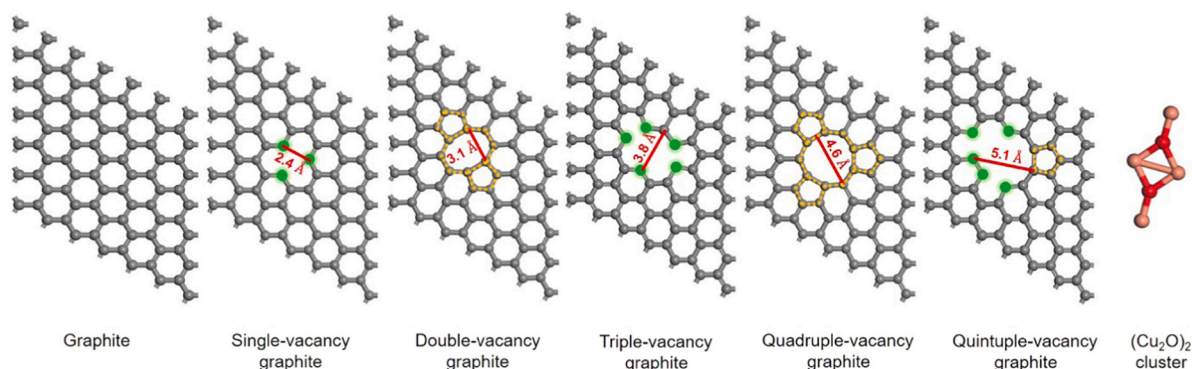


Fig. 7. Optimized structures of graphite, vacancy-type defects on graphite and (Cu₂O)₂ cluster.

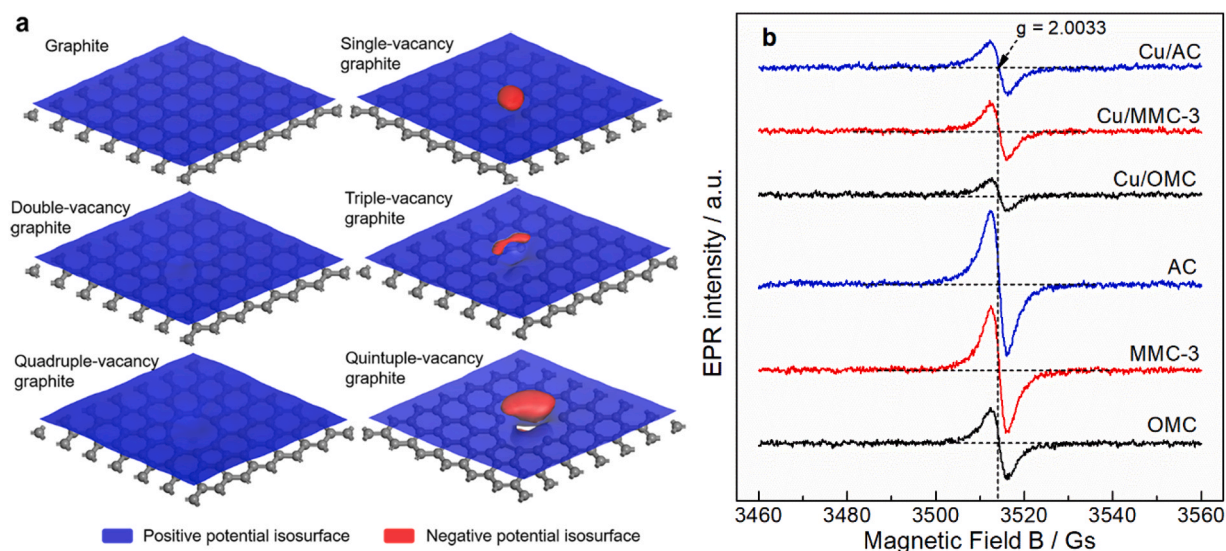


Fig. 8. (a) Electrostatic potential isosurfaces (at 0.008 a.u.) on the graphite layer and (b) the first-derivative X-band EPR spectra of OMC, MMC-3, AC supports and their corresponding catalysts.

spectrum. The normalized X-ray absorption near edge structure (XANES) spectra of the as-prepared catalyst and standard samples are shown on Fig. 9a. It is clearly witnessed that both the line shape and peak location of Cu/MMC-3 catalyst are much consistent with the characteristic absorptions of bulk Cu_2O . It reveals that most of Cu species in the catalyst was in form of Cu_2O . As shown in the EXAFS spectra in *R* space on Fig. 9b, two distinct scatterings of Cu/MMC-3 catalyst at 1.5 Å and 2.7 Å are corresponding to the first shell of Cu-C/O [49] and the second shell of Cu-Cu, respectively. It is noted that to distinguish the absorption of Cu-C shell from Cu-O shell at EXAFS spectrum is very difficult, because of the similar EXAFS phase shifts and backscattering amplitude functions of carbon and oxygen atom [50]. However, the coordination number (CN) of Cu-C/O shell is calculated as 4.32 by fitting the EXAFS spectra with optimized curvefit parameters listed in Table S3. This coordination number is excessive to the theoretical value of 2 for pure Cu_2O . It suggests the coordination number of the Cu-C bonding between Cu_2O nanoparticle and micropore-rich carbon support is about 2. The result is almost consistent with the as-optimized configuration of $(\text{Cu}_2\text{O})_2$ /carbon substrate system by DFT calculation, as shown in Fig. S7.

The reactivity of the carbon atom on all pristine and defective surface is analyzed based on the escape energy for carbon atom from the substrate. It is found that the escape energy for carbon atom on the defective surface decreased significantly by comparing to that on perfect graphite sheet, as shown in Table 3. Especially on the single and triple vacancy, the escape energy for the under-coordinated carbon atom is approximately equal to half of that for saturated atom on graphite surface. It suggests that the under-coordinated carbon atom is more easily released to reduce CuO than the saturated one. This is also testified by the fact that the temperature needed for CuO auto-reducing to Cu_2O on crystalline CNT lack of defects is higher than that on OMC and AC [15].

The binding energy of $(\text{Cu}_2\text{O})_2$ cluster supported on the defective carbon surfaces is stronger than that supported on the pristine graphite surface, as shown in Table 3. It suggests that the defects are beneficial for the immobilization of $(\text{Cu}_2\text{O})_2$ clusters. Besides, the population analysis of the Hirshfeld charge (Table 3) shows that the charge from $(\text{Cu}_2\text{O})_2$ cluster to defective graphite substrates increases obviously by comparing with that to graphite substrate. And this charge transfer is consistent with the $\text{Cu}_{2p3/2}$ peak shift to relatively high binding energy in XPS spectrum due to the introduction of micropores. This is likely to be attributed to the increase electron attraction ability of defective carbon surface, which can be reflected from the enhanced electrostatic

potential energy (ESPE) of defective graphite than pristine graphite, as shown in Table 3. The phenomenon is also agreed with the reported results on the electron transfer between monatomic Cu and defective graphene sheet [26].

Based on the discussion of experimental and computational results, a mechanism of nano Cu_2O catalyst formed on the micropore-rich carbon support is proposed, as shown in Fig. 10. Firstly, introducing micropores virtually cause vacancy-type defects in the carbon material, which was endowed with numerous under-coordinated carbon atoms. During impregnation, the under-coordinated carbon atoms provide such a negative potential region due to the dangling bonds that $\text{Cu}(\text{H}_2\text{O})_4^{2+}$ ions are induced to pair the dangling bonds on the under-coordinated carbon atoms and form Cu-C bond at the interface. Since the diameter of $\text{Cu}(\text{H}_2\text{O})_4^{2+}$ ion (1.5 nm) far exceeds the pore size of as-formed micropores (0.4 nm), the $\text{Cu}(\text{H}_2\text{O})_4^{2+}$ ions cannot enter the micropores but located at the micropore mouth. When the impregnated mixture is drying, dissociative H^+ ions in water combining with some NO_3^- ions to form HNO_3 molecules evaporate away and residual OH^- is generated $\text{Cu}_2(\text{OH})_3\text{NO}_3$ on the carbon surface. During calcination, $\text{Cu}_2(\text{OH})_3\text{NO}_3$ thermally decompose to CuO nanoparticles at about 200 °C. Subsequently, CuO are gradually auto-reduced to Cu_2O by the under-coordinated carbon atom with further raising temperature up to 300 °C. The high microporosity gives rise to a high concentration of these reactive carbon atoms, which significantly accelerate the reduction of CuO to Cu_2O in kinetics at early reaction. Meantime, the swift transformation of crystalline phase during the rapid auto-reduction facilitate the diffusion of lattice oxygen to the surface for deep reduction and thus give rise to a high percentage of Cu_2O in the entire nanoparticles. When the original under-coordinated carbon atoms at the micropore mouth are consumed, the adjoining carbon atoms will be under-coordinated further and bind with copper atom of Cu_2O nanoparticles, which accounts for the stabilization of Cu_2O on the carbon materials rich of micropores. This action maybe result in broadening of the micropore mouth and embedded Cu_2O nanoparticles. In conclusion, the micropores in the porous carbon materials facilitate the formation and stabilization of Cu_2O nanoparticles.

4. Conclusions

Micropores were introduced into ordered mesoporous carbon by KOH etching to fabricate a micropore-rich mesoporous carbon, which is further used as support to prepare a highly active Cu_2O catalyst for

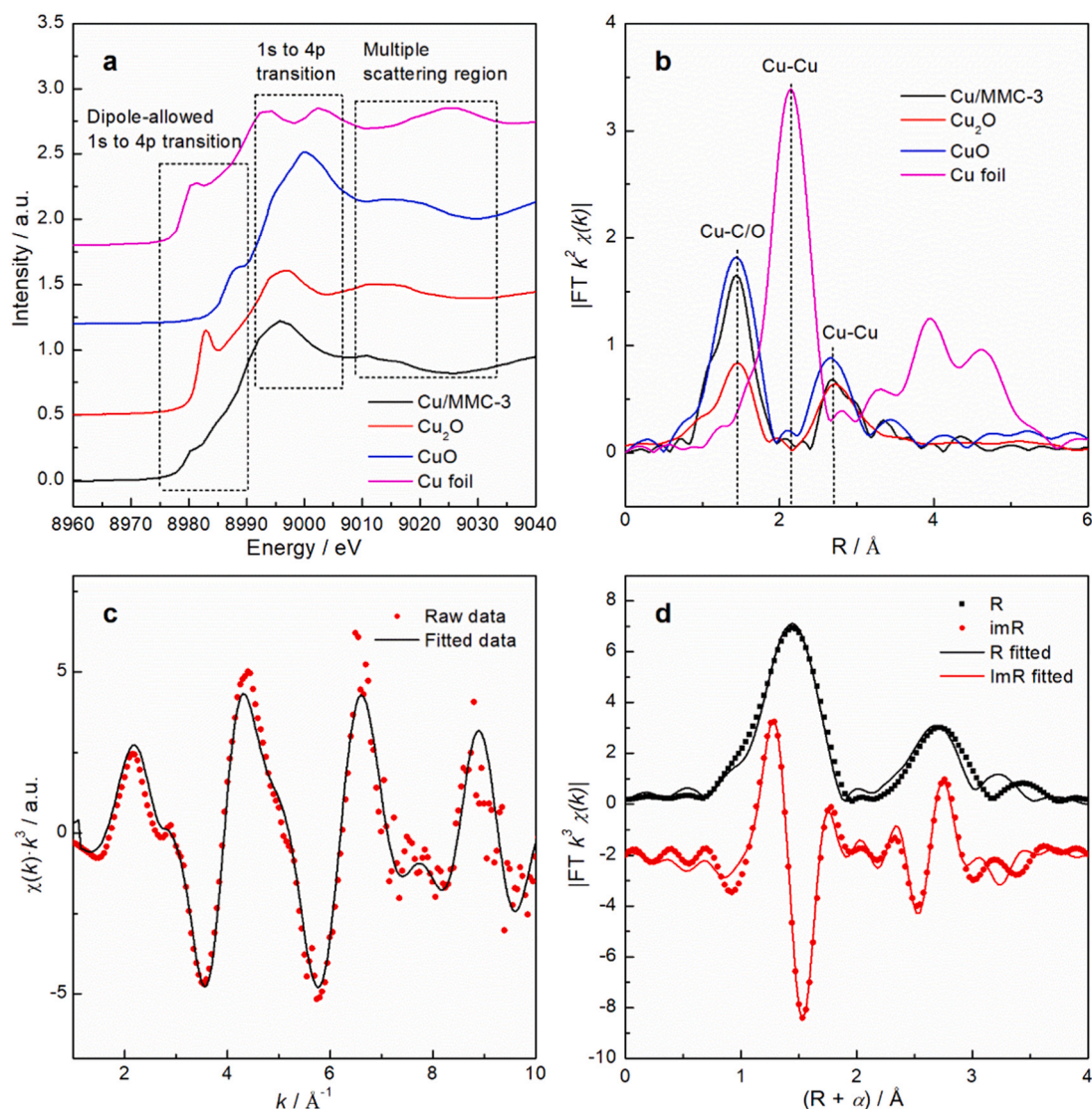


Fig. 9. Synchrotron XAFS measurements of Cu/MMC-3 catalyst. (a) Cu K-edge XANES profiles for Cu/MMC-3 catalyst, Cu₂O, CuO and Cu foil. (b) Cu K-edge EXAFS spectra in R space for Cu/MMC-3 catalyst, Cu₂O, CuO and Cu foil. (c) Cu K-edge EXAFS (points) and the curvefit (line) for Cu/MMC-3 catalyst, shown in k^3 weighted k -space. (d) Cu K-edge EXAFS (points) and the curvefit (line) for Cu/MMC-3 catalyst, shown in R -space (FT magnitude and imaginary component). The data are k^3 weighted and not phase-corrected.

Table 3

Results of DFT calculations carried on carbon substrates and (Cu₂O)₂/carbon substrates.

Models (Cu ₂ O) ₂ /carbon substrate	ESPE _{carbon} ^a (Ha)	EE _C ^b (kJ mol ⁻¹)	BE _{Cu₂O} ^c (kJ mol ⁻¹)	Q ₂ ^d (Cu ₂ O)
(Cu ₂ O) ₂ /Graphite	4.5968	1444.6	-341.4	0.2851
(Cu ₂ O) ₂ /Single-vacancy graphite	5.1959	732.1	-502.4	0.3552
(Cu ₂ O) ₂ /Double-vacancy graphite	5.7768	1072.9	-443.6	0.5901
(Cu ₂ O) ₂ /Triple-vacancy graphite	6.0097	771.2	-636.6	0.3597
(Cu ₂ O) ₂ /Quadruple-vacancy graphite	6.6722	1150.2	-685.5	0.4382
(Cu ₂ O) ₂ /Quintuple-vacancy graphite	6.6311	1053.7	-1007.6	0.4625

^a Electrostatic potential energy of carbon substrates. ^b Escape energy for a carbon atom at the carbon substrates. ^c Binding energy of (Cu₂O)₂ on carbon substrates. ^d Electron transfer from (Cu₂O)₂ to the substrates.

improving catalytic activity of methanol oxidation carbonylation. The microporosity was adjusted by controlled the KOH/OMC mass ratio to investigate the role of the micropores. It is found that introducing micropores causes vacancy-type defects at graphite crystallite in the framework of the carbon support, which is thus endowed with plentiful under-coordinated carbon atoms. These atoms serve to bind Cu(H₂O)₄²⁺ precursors to form well-dispersed Cu nanoparticles at the large ordered mesopore surface in one aspect. In the second, increasing the number of the under-coordinated carbon atoms by increasing microporosity accelerate the auto-reducing rate of CuO to Cu₂O in kinetics and further increase the limit of the auto-reduction to form high-purity Cu₂O in both surface and bulk of the nanoparticles. Last but not the least, the micropores facilitate electron transfer from Cu₂O nanoparticles to the carbon support, resulting in electron-deficient environment of the active Cu⁺ sites, which is a new finding to improve the intrinsic activity of the active Cu⁺ site in methanol oxidation carbonylation. All aspects of the good dispersion, high purity and electron-deficient environment of the Cu₂O nanoparticles give rise to high yield of DMC. Besides, this work suggests a way to prepare a highly efficient nano Cu₂O catalyst, which is potential in extensive catalytic applications, such as photo-

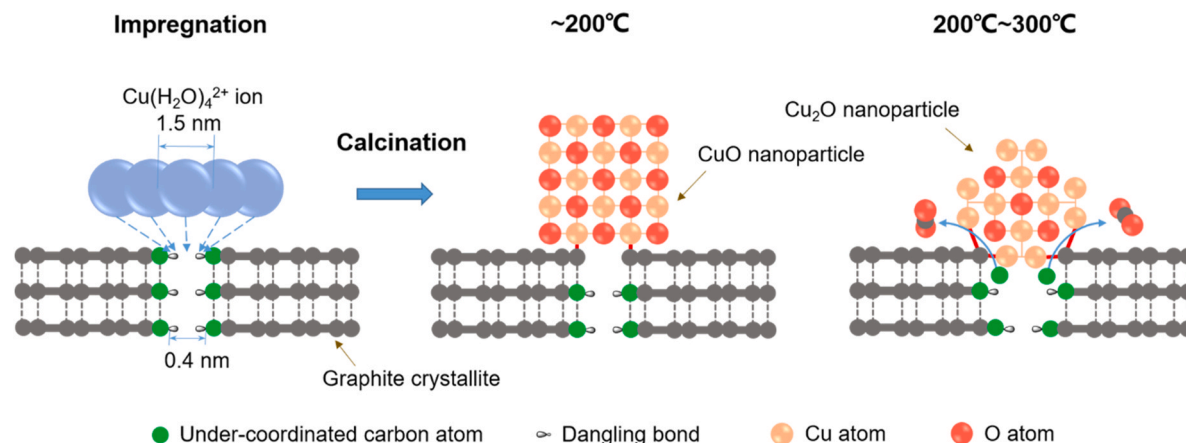


Fig. 10. Formation mechanism of nano Cu_2O catalysts on the micropore-rich carbon support.

dehydrogenation, electro-reduction, sensing and so on.

CRediT authorship contribution statement

Jiajun Wang: Conceptualization, Methodology, Software, Investigation, Writing – original draft, Formal analysis, Visualization. **Tingjun Fu:** Data curation. **Fanhui Meng:** Data curation. **Dan Zhao:** Assisted characterizations. **Steven S. C. Chuang:** Writing – review & editing. **Zhong Li:** Supervision, Project administration, Funding acquisition, Resources, Writing – review & editing.

Acknowledgment

This work was supported by the National Natural Science Foundation of China (U1510203); and the Key Research and Development Project of Shanxi Province (International Science and Technology Cooperation Program) (201803D421011). The authors are grateful to Prof. Huayan Zheng, Guoqiang Zhang, Mingsheng Luo and Dr. Nilesh Narkhede for their kindly academic discussion and language help.

Declaration of Competing Interest

The authors declare that they have no known competing financial interests or personal relationships that could have appeared to influence the work reported in this paper.

Appendix A. Supporting information

Supplementary data associated with this article can be found in the online version at [doi:10.1016/j.apcatb.2021.120890](https://doi.org/10.1016/j.apcatb.2021.120890).

References

- [1] M. Selva, A. Perosa, Green chemistry metrics: a comparative evaluation of dimethyl carbonate, methyl iodide, dimethyl sulfate and methanol as methylating agents, *Green. Chem.* 10 (2008) 457, <https://doi.org/10.1039/b713985c>.
- [2] Z. Yang, L. Liu, H. An, C. Li, Z. Zhang, W. Fang, F. Xu, S. Zhang, Cost-effective synthesis of high molecular weight biobased polycarbonate via melt polymerization of isosorbide and dimethyl carbonate, *ACS Sustain. Chem. Eng.* 8 (2020) 9968–9979, <https://doi.org/10.1021/acssuschemeng.0c00430>.
- [3] M.O. Sonnat, S. Amigoni, E.P. Taffin de Givenchy, T. Darmanin, O. Choulet, F. Guittard, Glycerol carbonate as a versatile building block for tomorrow: synthesis, reactivity, properties and applications, *Green. Chem.* 15 (2013) 283–306, <https://doi.org/10.1039/c2gc36525a>.
- [4] A.O. Esan, A.D. Adeyemi, S. Ganesan, A review on the recent application of dimethyl carbonate in sustainable biodiesel production, *J. Clean. Prod.* 257 (2020), 120561, <https://doi.org/10.1016/j.jclepro.2020.120561>.
- [5] L. Razzaq, M.A. Mujtaba, M.E.M. Soudagar, W. Ahmed, H. Fayaz, S. Bashir, I.M. R. Fattah, H.C. Ong, K. Shahpurkar, A. Afzal, S. Wageh, A. Al-Ghamdi, M.S. Ali, A. I. El-Seesy, Engine performance and emission characteristics of palm biodiesel blends with graphene oxide nanoplatelets and dimethyl carbonate additives, *J. Environ. Manage.* 282 (2021), 111917, <https://doi.org/10.1016/j.jenvman.2020.111917>.
- [6] S.-H. Pyo, J.H. Park, T.-S. Chang, R. Hatti-Kaul, Dimethyl carbonate as a green chemical, *Curr. Opin. Green. Sust.* 5 (2017) 61–66, <https://doi.org/10.1016/j.cogsc.2017.03.012>.
- [7] H.-Z. Tan, Z.-Q. Wang, Z.-N. Xu, J. Sun, Y.-P. Xu, Q.-S. Chen, Y. Chen, G.-C. Guo, Review on the synthesis of dimethyl carbonate, *Catal. Today* 316 (2018) 2–12, <https://doi.org/10.1016/j.cattod.2018.02.021>.
- [8] S. Huang, B. Yan, S. Wang, X. Ma, Recent advances in dialkyl carbonates synthesis and applications, *Chem. Soc. Rev.* 44 (2015) 3079–3116, <https://doi.org/10.1039/C4CS00374H>.
- [9] R. Jiang, Y. Wang, X. Zhao, S. Wang, C. Jin, C. Zhang, Characterization of catalyst in the synthesis of dimethyl carbonate by gas-phase oxidative carbonylation of methanol, *J. Mol. Catal. A: Chem.* 185 (2002) 159–166, [https://doi.org/10.1016/S1381-1169\(01\)00526-X](https://doi.org/10.1016/S1381-1169(01)00526-X).
- [10] M. Richter, M.J.G. Fait, R. Eckelt, E. Schreier, M. Schneider, M.M. Pohl, R. Fricke, Oxidative gas phase carbonylation of methanol to dimethyl carbonate over chloride-free Cu-impregnated zeolite Y catalysts at elevated pressure, *Appl. Catal. B* 73 (2007) 269–281, <https://doi.org/10.1016/j.apcatb.2006.11.015>.
- [11] G. Zhang, Z. Li, H. Zheng, T. Fu, Y. Ju, Y. Wang, Influence of the surface oxygenated groups of activated carbon on preparation of a nano Cu/AC catalyst and heterogeneous catalysis in the oxidative carbonylation of methanol, *Appl. Catal. B* 179 (2015) 95–105, <https://doi.org/10.1016/j.apcatb.2015.05.001>.
- [12] X. Wang, T. Fu, H. Zheng, G. Zhang, Z. Li, The influence of the pore structure in ordered mesoporous carbon over the formation of Cu species and their catalytic activity towards the methanol oxidative carbonylation, *J. Mater. Sci.* 51 (2016) 1–15, <https://doi.org/10.1007/s10853-016-9857-z>.
- [13] T. Fu, X. Wang, H. Zheng, Z. Li, Effect of Cu location and dispersion on carbon sphere supported Cu catalysts for oxidative carbonylation of methanol to dimethyl carbonate, *Carbon* 115 (2017) 363–374, <https://doi.org/10.1016/j.carbon.2017.01.004>.
- [14] Z. Li, C.M. Wen, R.Y. Wang, H.Y. Zheng, K.C. Xie, Chloride-free $\text{Cu}_2\text{O}/\text{AC}$ catalyst prepared by pyrolysis of copper acetate and catalytic oxycarbonylation, *Chem. J. Chin. Univ.* 30 (2009) 2024–2031, <https://doi.org/10.3321/j.issn:0251-0790.2009.10.021>.
- [15] D. Zhao, G. Zhang, L. Yan, L. Kong, H. Zheng, J. Mi, Z. Li, Carbon nanotube-supported Cu-based catalysts for oxidative carbonylation of methanol to methyl carbonate: effect of nanotube pore size, *Catal. Sci. Technol.* 10 (2020) 2615–2626, <https://doi.org/10.1039/c9cy02407g>.
- [16] S. Jun, S.H. Joo, R. Ryoo, M. Kruk, M. Jaroniec, Z. Liu, T. Ohsuna, O. Terasaki, Synthesis of new, nanoporous carbon with hexagonally ordered mesostructure, *J. Am. Chem. Soc.* 122 (2000) 10712–10713, <https://doi.org/10.1021/ja002261e>.
- [17] J. Wang, S. Kaskel, KOH activation of carbon-based materials for energy storage, *J. Mater. Chem.* 22 (2012) 23710, <https://doi.org/10.1039/c2jm34066f>.
- [18] M.A. Lillo-Ródenas, D. Cazorla-Amorós, A. Linares-Solano, Understanding chemical reactions between carbons and NaOH and KOH An insight into the chemical activation mechanism, *Carbon* 41 (2003) 267–275, [https://doi.org/10.1016/S0008-6223\(02\)00279-8](https://doi.org/10.1016/S0008-6223(02)00279-8).
- [19] Y. Lv, F. Zhang, Y. Dou, Y. Zhai, J. Wang, H. Liu, Y. Xia, B. Tu, D. Zhao, A comprehensive study on KOH activation of ordered mesoporous carbons and their supercapacitor application, *J. Mater. Chem.* 22 (2012) 93–99, <https://doi.org/10.1039/c1jm12742j>.
- [20] J. Ren, M.J. Ren, D.L. Wang, J.Y. Lin, Z. Li, Mechanism of microwave-induced carbothermic reduction and catalytic performance of Cu/activated carbon catalysts in the oxidative carbonylation of methanol, *J. Therm. Anal. Calorim.* 120 (2015) 1929–1939, <https://doi.org/10.1007/s10973-015-4519-y>.
- [21] B. Ravel, M. Newville, Athena, Artemis, Hephaestus: data analysis for X-ray absorption spectroscopy using IFEFFIT, *J. Synchrotron Radiat.* 12 (2005) 537–541, <https://doi.org/10.1107/S0909049505012719>.
- [22] J. Ren, P. Hao, W. Sun, R. Shi, S. Liu, Ordered mesoporous silica-carbon-supported copper catalyst as an efficient and stable catalyst for catalytic oxidative

- carbonylation, *Chem. Eng. J.* 328 (2017) 673–682, <https://doi.org/10.1016/j.cej.2017.07.101>.
- [23] M. Jdraque, M. Martin, DFT calculations of $\text{Cu}_n\text{O}_m^{0/+}$ clusters: evidence for Cu_2O building blocks, *Chem. Phys. Lett.* 456 (2008) 51–54, <https://doi.org/10.1016/j.cplett.2008.02.114>.
- [24] F. Yang, Q. Sun, L.L. Ma, Y. Jia, S.J. Luo, J.M. Liu, W.T. Geng, J.Y. Chen, S. Li, Y. Yu, Magnetic properties of Cu_nO_m clusters: a first principles study, *J. Phys. Chem. A* 114 (2010) 8417–8422, <https://doi.org/10.1021/jp103703n>.
- [25] T. You, L. Jiang, P. Yin, Y. Shang, D. Zhang, L. Guo, S. Yang, Direct observation of p,p'-dimercaptoazobenzene produced from p-aminothiophenol and p-nitrothiophenol on Cu_2O nanoparticles by surface-enhanced Raman spectroscopy, *J. Raman Spectrosc.* 45 (2014) 7–14, <https://doi.org/10.1002/jrs.4411>.
- [26] W. Sun, R. Shi, X. Wang, S. Liu, X. Han, C. Zhao, Z. Li, J. Ren, Density-functional theory study of dimethyl carbonate synthesis by methanol oxidative carbonylation on single-atom Cu_1 /graphene catalyst, *Appl. Surf. Sci.* 425 (2017) 291–300, <https://doi.org/10.1016/j.apsusc.2017.07.002>.
- [27] R. Ryoo, S.H. Joo, M. Kruk, M. Jaroniec, Ordered mesoporous carbons, *Adv. Mater.* 13 (2001) 677–681, [https://doi.org/10.1002/1521-4095\(200105\)13:9%3C677::AID-ADMA677%3E3.0.CO;2-C](https://doi.org/10.1002/1521-4095(200105)13:9%3C677::AID-ADMA677%3E3.0.CO;2-C).
- [28] J. Cai, X. Hu, B. Xiao, Y. Zhou, W. Wei, Recent developments on fractal-based approaches to nanofluids and nanoparticle aggregation, *Int. J. Heat. Mass Transf.* 105 (2017) 623–637, <https://doi.org/10.1016/j.ijheatmasstransfer.2016.10.011>.
- [29] J. Fujita, K. Nakamoto, M. Kobayashi, Infrared spectra of metallic complexes. II. The absorption bands of coordinated water in Aquo complexes, *J. Am. Chem. Soc.* 78 (1956) 3963–3965, <https://doi.org/10.1021/ja01597a026>.
- [30] R. Kaiser, A. Kulczyk, D. Rich, R.J. Willey, J. Minicucci, B. MacIver, Effect of pore size distribution of commercial activated carbon fabrics on the adsorption of CWA simulants from the liquid phase, *Ind. Eng. Chem. Res.* 46 (2007) 6126–6132, <https://doi.org/10.1021/ie061429n>.
- [31] D. Wang, G.H. Yang, Q.X. Ma, M.B. Wu, Y.S. Tan, Y. Yoneyama, N. Tsubaki, Confinement effect of carbon nanotubes: copper nanoparticles filled carbon nanotubes for hydrogenation of methyl acetate, *ACS Catal.* 2 (2012) 1958–1966, <https://doi.org/10.1021/cs300234e>.
- [32] K. Tomishige, T. Sakai, S.-i. Sakai, K. Fujimoto, Dimethyl carbonate synthesis by oxidative carbonylation on activated carbon supported CuCl_2 catalysts: catalytic properties and structural change, *Appl. Catal. A* 181 (1999) 95–102, [https://doi.org/10.1016/S0926-860X\(98\)00386-X](https://doi.org/10.1016/S0926-860X(98)00386-X).
- [33] Z. Riguang, L. Hongyan, L. Lixia, L. Zhong, W. Baojun, A. DFT, study on the formation of CH_3O on $\text{Cu}_2\text{O}(111)$ surface by CH_3OH decomposition in the absence or presence of oxygen, *Appl. Surf. Sci.* 257 (2011) 4232–4238, <https://doi.org/10.1016/j.apsusc.2010.12.026>.
- [34] S.T. King, Reaction mechanism of oxidative carbonylation of methanol to dimethyl carbonate in Cu–Y zeolite, *J. Catal.* 161 (1996) 530–538, <https://doi.org/10.1006/jcat.1996.0215>.
- [35] S.A. Anderson, T.W. Root, Investigation of the effect of carbon monoxide on the oxidative carbonylation of methanol to dimethyl carbonate over Cu^+X and $\text{Cu}^{2+}\text{ZSM-5}$ zeolites, *J. Mol. Catal. A: Chem.* 220 (2004) 247–255, <https://doi.org/10.1016/j.molcata.2004.06.006>.
- [36] R. Zhang, L. Song, B. Wang, Z. Li, A density functional theory investigation on the mechanism and kinetics of dimethyl carbonate formation on Cu_2O catalyst, *J. Comput. Chem.* 33 (2012) 1101–1110, <https://doi.org/10.1002/jcc.22939>.
- [37] V. Schwartz, A. Campos, A. Egbebi, J.J. Spivey, S.H. Overbury, EXAFS and FT-IR characterization of Mn and Li promoted titania-supported Rh catalysts for CO hydrogenation, *ACS Catal.* 1 (2011) 1298–1306, <https://doi.org/10.1021/cs200281g>.
- [38] D.F. Cox, K.H. Schulz, Interaction of CO with Cu^+ cations: CO adsorption on Cu_2O (100), *Surf. Sci.* 249 (1991) 138–148, [https://doi.org/10.1016/0039-6028\(91\)90839-K](https://doi.org/10.1016/0039-6028(91)90839-K).
- [39] R. Shi, J. Zhao, S. Liu, W. Sun, H. Li, P. Hao, Z. Li, J. Ren, Nitrogen-doped graphene supported copper catalysts for methanol oxidative carbonylation: enhancement of catalytic activity and stability by nitrogen species, *Carbon* 130 (2018) 185–195, <https://doi.org/10.1016/j.carbon.2018.01.011>.
- [40] B.M. Rosen, X. Jiang, C.J. Wilson, N.H. Nguyen, M.J. Monteiro, V. Percec, The disproportionation of $\text{Cu}(\text{I})\text{X}$ mediated by ligand and solvent into $\text{Cu}(\text{I})$ and $\text{Cu}(\text{II})\text{X}_2$ and its implications for SET-LRP, *J. Polym. Sci. Part A: Polym. Chem.* 47 (2009) 5606–5628, <https://doi.org/10.1002/pola.23690>.
- [41] Z. Zhang, H. Wu, Z. Yu, R. Song, K. Qian, X. Chen, J. Tian, W. Zhang, W. Huang, Site-resolved Cu_2O catalysis in the oxidation of CO, *Angew. Chem. Int. Ed.* 58 (2019) 4276–4280, <https://doi.org/10.1002/anie.201814258>.
- [42] K.J.J. Mayrhofer, B.B. Blizanac, M. Arenz, V.R. Stamenkovic, P.N. Ross, N. M. Markovic, The impact of geometric and surface electronic properties of Pt-catalysts on the particle size effect in electrocatalysis, *J. Phys. Chem. B* 109 (2005) 14433–14440, <https://doi.org/10.1021/jp051735z>.
- [43] G. Zhang, Z. Li, H. Zheng, Z. Hao, X. Wang, J. Wang, Influence of surface oxygenated groups on the formation of active Cu species and the catalytic activity of Cu/AC catalyst for the synthesis of dimethyl carbonate, *Appl. Surf. Sci.* 390 (2016) 68–77, <https://doi.org/10.1016/j.apsusc.2016.08.054>.
- [44] T. Kimura, Molten salt synthesis of ceramic powders, in: C. Sikalidis (Ed.), *Advances in Ceramics - Synthesis and Characterization, Processing and Specific Applications*, INTECH Open Access Publisher, New York, 2011, pp. 75–100.
- [45] M.E. Brown, D. Dollimore, A.K. Galwey, *Reactions in the Solid State*, in: C. H. Bamford, C.F.H. Tipper (Eds.), *Comprehensive Chemical Kinetics*, Elsevier, Amsterdam, 1980, pp. 1–340.
- [46] J.A. Hedvall, Changes in crystal structure and their influence on the reactivity and catalytic effect of solids, *Chem. Rev.* 15 (1934) 139–168, <https://doi.org/10.1021/cr60051a001>.
- [47] F. Banhart, J. Kotakoski, A.V. Krashenninnikov, Structural defects in graphene, *ACS Nano* 5 (2011) 26–41, <https://doi.org/10.1021/nn102598m>.
- [48] C.V. Pham, M. Krueger, M. Eck, S. Weber, E. Erdem, Comparative electron paramagnetic resonance investigation of reduced graphene oxide and carbon nanotubes with different chemical functionalities for quantum dot attachment, *Appl. Phys. Lett.* 104 (2014), 132102, <https://doi.org/10.1063/1.4870297>.
- [49] F. Huang, Y. Deng, Y. Chen, X. Cai, M. Peng, Z. Jia, J. Xie, D. Xiao, X. Wen, N. Wang, Z. Jiang, H. Liu, D. Ma, Anchoring Cu_1 species over nanodiamond-graphene for semi-hydrogenation of acetylene, *Nat. Commun.* 10 (2019) 4431, <https://doi.org/10.1038/s41467-019-12460-7>.
- [50] M.K. Neylon, C.L. Marshall, A.J. Kropf, In situ EXAFS analysis of the temperature-programmed reduction of Cu-ZSM-5, *J. Am. Chem. Soc.* 124 (2002) 5457–5465, <https://doi.org/10.1021/ja0176696>.